Mathematical Biosciences and Engineering

https://www.aimspress.com/journal/mbe

MBE, 23(5): 1402–1436.
DOI: 10.3934/mbe.2026052
Received: 01 February 2026
Revised: 12 March 2026
Accepted: 30 March 2026
Published: 13 April 2026

Research article

A stochastic agent-based model for simulating tumor–immune dynamics and evaluating therapeutic strategies

Yuhong Zhang[1], Chenghang Li[2], Boya Wang[2] and Jinzhi Lei[2,3,*]

[1] School of Software, Tiangong University, Tianjin 300387, China

[2] School of Mathematical Sciences, Tiangong University, Tianjin 300387, China

[3] Center for Applied Mathematics, Tiangong University, Tianjin 300387, China

* **Correspondence:** Email: jzlei@tiangong.edu.cn.

Abstract: Tumor–immune interactions are central to understanding cancer progression and treatment outcomes. In this study, we present a stochastic agent-based model that integrates cellular heterogeneity, spatial cell–cell interactions, and the evolution of drug resistance to simulate tumor growth and the immune response in a two-dimensional microenvironment. This model captures the dynamic behaviors of four major cell types, specifically tumor cells, cytotoxic T lymphocytes, helper T cells, and regulatory T cells, and incorporates key biological processes, including proliferation, apoptosis, migration, and immune regulation. Using this framework, we simulate tumor progression under different therapeutic interventions, including radiotherapy, targeted therapy, and immune checkpoint blockade. Our simulations reproduce emergent phenomena such as immune privilege and spatial immune exclusion. Quantitative analyses demonstrate that all therapies suppress tumor growth to varying degrees and reshape the tumor microenvironment. Notably, combination therapies, particularly targeted therapy with immunotherapy, achieve the most effective tumor control. Crucially, sensitivity analyses reveal a distinct hierarchy among therapeutic determinants: Short-term efficacy is predominantly governed by intrinsic drug sensitivity thresholds rather than drug resistance update rates. Furthermore, we identify a response saturation effect that is specific to immunotherapy, where efficacy plateaus beyond a certain sensitivity threshold due to the spatial limits of immune infiltration. This work demonstrates the utility of agent-based models in capturing complex tumor–immune dynamics and provides a computational platform for optimizing cancer treatment strategies. The model is extensible, biologically interpretable, and well-suited for future integration with experimental or clinical data.

Keywords: agent-based model; tumor–immune interactions; cellular heterogeneity; tumor drug resistance

1. Introduction

Tumor–immune interactions and tumor heterogeneity are fundamental to understanding cancer progression and treatment outcomes. The adaptive immune system, particularly T cell-mediated immunity, enables targeted tumor clearance through antigen-specific recognition [1, 2]. However, tumor cells evade these responses through multiple mechanisms, including antigen presentation defects, immunosuppressive microenvironment formation, and immune checkpoint activation [3, 4]. Compounding this challenge, tumor heterogeneity manifests as diverse genetic, phenotypic, and functional variations that shape cellular networks within the tumor microenvironment (TME) [5–7]. This heterogeneity drives therapeutic resistance through clonal evolution, enabling selective expansion of resistant subpopulations under treatment pressure [8]. Resistance mechanisms include drug target mutations, apoptosis suppression, and therapy-induced epigenetic alterations [9–11]. A quantitative understanding of these interconnected dynamics is therefore essential for elucidating immune evasion and resistance mechanisms and for developing more effective therapeutic strategies.

Agent-based modeling (ABM) is a stochastic computational approach that decomposes systems into autonomous, heterogeneous agents. Each agent interacts with its environment and with other agents through predefined local rules and decision-making mechanisms. These microscopic interactions collectively give rise to macroscopic system behaviors. This framework enables the quantitative study of dynamic evolution in complex systems [12, 13]. ABM effectively captures a system's heterogeneity, stochasticity, and nonlinearity. It is therefore particularly suitable for studying multiscale complex systems and has been widely applied in computational and systems biology [14–16].

In recent years, ABM has made significant progress in tumor research. Anderson et al. [17] integrated partial differential equations with cellular automata to model the effects of the extracellular matrix and oxygen concentration, revealing how microenvironmental selection pressures can drive phenotypic evolution. Zhang et al. [18] used ABM to characterize epidermal growth factor receptor-driven molecular networks, simulating glioma's growth and invasion. Stamatakos et al. [19] developed the technologically integrated Oncosimulator, a simulation platform that combines multiscale cancer modeling with information technology. By simulating the response of nephroblastoma and breast cancer to neoadjuvant chemotherapy within a clinical trial context, their work demonstrated the potential of multiscale models for clinical adaptation and validation. Gong et al. [20] developed a multiscale ABM incorporating heterogeneous immune checkpoint expression to simulate spatiotemporal tumor–immune interactions under immune checkpoint inhibitor therapy. Jalalimanesh et al. [21] established a multiscale ABM to simulate vascularized tumor growth and radiotherapy response. Legaria-Peña et al. [22–24] constructed cellular automaton models through a series of studies to systematically explore the complex interactions among tumor growth, immune regulation, and vascular networks.

In this study, we developed an ABM that incorporates cellular heterogeneity and tumor drug resistance to simulate the complex interactions among tumor cells and cytotoxic T cells (CTLs), helper T cells (Th cells), and regulatory T cells (Tregs). For each cell type, we defined behavioral rules and mathematical formulations of the cell state transition rates, including proliferation, death, and migration. This study establishes a reliable computational framework as a foundation for subsequent biological applications. Within this framework, we simulated the spatiotemporal evolution and the drug resistance dynamics of heterogeneous tumors under three treatment modalities, namely radiotherapy, targeted therapy, and immunotherapy.

Compared with the existing tumor–immune ABM studies mentioned above, this work achieves three key advancements in model construction. First, we expand the representation of T cell subsets. Previous studies, such as Surendran et al., modeled interactions between tumor cells and CD8+ T cells, revealing how spatial heterogeneity influences the treatment response in glioblastoma [25]. This study builds on that foundation by incorporating regulatory T cells, creating a more comprehensive framework to characterize the tumor–immune interaction network. Second, we introduce a novel approach to quantify cellular heterogeneity. These measurable indicators are directly embedded into cellular behavioral rules, enabling systematic characterization of the functional states of distinct cell types. Third, we advance the simulation of therapeutic interventions. While recent studies have used ABMs to simulate multiple treatment modalities [26], this work not only evaluates various standard therapies and their combinations within a unified framework, but also integrates dynamic drug resistance metrics. This integration tracks the evolution of resistance over time and provides a new perspective for optimizing combination treatment strategies.

The simulation results revealed the complex dynamic equilibrium between tumor and immune cells and recapitulated the phenomenon of immune privilege. We further contrasted different therapeutic strategies, demonstrating that radiotherapy suppressed tumor growth, reduced volume and cell density, attenuated Treg-mediated immunosuppression, enhanced CTL infiltration, and improved the TME. Targeted therapy effectively killed tumor cells and enhanced antitumor immunity by boosting T cell proliferation. Immunotherapy restricted tumor expansion by enhancing the immune response and activating T cells' function. Comparative analysis indicated that targeted therapy accelerated the selection of drug-resistant clones, whereas immunotherapy preserved some sensitive subpopulations, suggesting that combined strategies might delay the onset of drug resistance. Evaluations of different therapeutic strategies demonstrated that combination therapies yielded significantly superior efficacy compared with monotherapies, particularly radiotherapy combined with targeted therapy, which shortened the treatment cycles and markedly improved the therapeutic outcomes. Finally, quantitative analysis revealed that while increasing the treatment intensity can enhance antitumor efficacy, an optimal threshold exists. This finding suggests that moderate intensification may improve outcomes, whereas excessive treatment ultimately disrupts the immune microenvironment's homeostasis.

The structure of this paper is organized as follows. Section 2 describes the simulator design, computational workflow, and model mechanisms. Section 3.1 presents tumor growth under immune surveillance without treatment. Sections 3.2 through 3.5 examine the tumor response, drug resistance dynamics, treatment efficacy, and intensity effects across different therapies. Section 4 summarizes the key findings, discusses the model's limitations, and outlines future directions.

2. Model and methods

2.1. Agent-based discrete stochastic simulation

In this study, we developed an agent-based discrete stochastic simulation scheme to model the spatiotemporal dynamics of tumor–immune system interactions and to evaluate the effects of different treatment strategies. The model uses a rectangular grid for spatial discretization (Figure 1). Although cell sizes exhibit heterogeneity in real biological systems, we simplify the model by assigning each cell to a single grid unit. This discretization enables local interactions between cells and their Moore neighborhood, balancing computational efficiency with spatial cell–cell interactions [27].

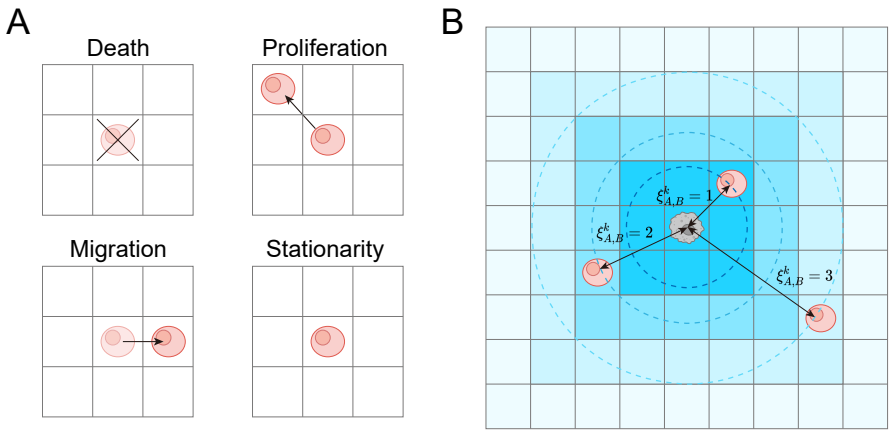

Figure 1. Schematic diagram of cell fate decision rules. (A) Cell behaviors within the Moore neighborhood include death, proliferation, migration, and quiescence. (B) The extended Moore neighborhood (blue dashed circle) comprises three concentric layers, with 8, 16, and 24 adjacent sites, respectively. The distance-dependent regulatory coefficients $1/\xi^k_{A,B}$ are assigned as 1, $1/2$, and $1/3$ from the innermost to the outermost layer.

We defined cell interaction neighborhoods using an extended Moore model with a radius of three cell layers (Figure 1B). This range captures biologically relevant local microenvironmental regulation, as intercellular effects diminish beyond this distance. It also avoids the excessive computational cost associated with larger neighborhoods. This configuration thus enables a comprehensive simulation of near-field intercellular interactions and supports large-scale modeling. When computing cell proliferation and death rates, the model incorporates influences from the other cells within three concentric layers around the target cell (Figure 1B). A distance-dependent regulatory mechanism is applied. For example, ξ^k_{C,T_C} denotes the distance between a tumor cell and a CTL, and $1/\xi^k_{C,T_C}$ serves as a distance-weighted regulatory coefficient in Eq (2.1) to quantify CTL-mediated killing. This mechanism captures the physiological distance-decay effect, where killing efficacy declines with increasing distance, enabling more realistic modeling of immune evasion.

At each time step Δt, every cell determines its fate on the basis of the transition rates and a uniform random number $r \in U(0,1)$ (Figure 2). For a given transition rate p (see Sections 2.2 and 2.3), the probability of a fate transition within Δt is $p \cdot \Delta t$. Depending on the value of r, the cell undergoes one of the following updates (Figures 1A and 2).

(1) Death. If $r < p^{id}_{dea} \cdot \Delta t$, the cell is removed and its grid unit becomes vacant.
(2) Proliferation. If at least one vacant position exists in the Moore neighborhood and $r < (p^{id}_{dea} + p^{id}_{pro}) \cdot \Delta t$, the cell proliferates. The original cell remains in place, and a daughter cell is generated in a randomly selected vacant adjacent grid cell (Figure 1A). The daughter cell inherits the parent's cell type and heterogeneity metrics. Detailed definitions are provided in Section 2.2.
(3) Migration. If a vacant neighboring position exists and $r < (p^{id}_{dea} + p^{id}_{pro} + p^{id}_{mig}) \cdot \Delta t$, the cell migrates to a randomly selected vacant Moore neighbor and updates its coordinates (Figure 1A). Migration is aborted if all the neighboring positions are occupied.
(4) Stationarity. If none of the above conditions are met, the cell remains quiescent, and its state is unchanged during the current time step.

The model is implemented in the C++ programming language and runs on both Linux and Microsoft Windows systems. The program workflow is shown in Figure 2 and Algorithm 1. The main steps are summarized below.

(1) System initialization. Read all parameter configuration files and set up the simulation environment.
(2) Cell placement. Tumor cells are positioned in the center of the space; immune cells are randomly placed around the tumor to simulate a solid tumor environment.
(3) Cell state update. At each time step Δt, one cell is randomly selected and updated according to the behavior rules and transition rates.
(4) Data recording. Key model outputs are recorded in real time, namely each cell's type, spatial coordinates, and heterogeneity metrics, with drug resistance specifically tracked for tumor cells, along with the counts of various cell types within the spatial domain.

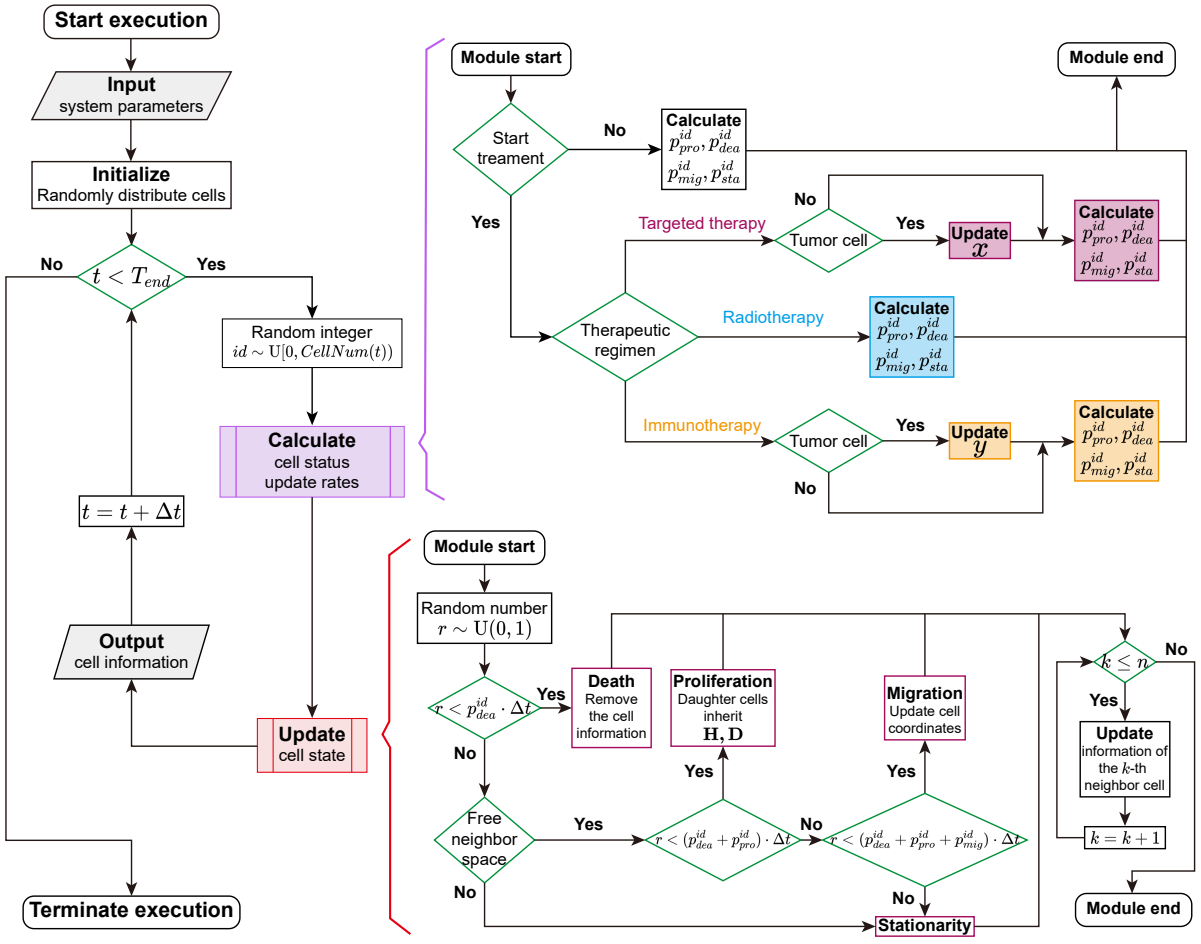

Figure 2. Stochastic simulation computational workflow. The left panel shows the main procedural framework. The two key modules used for calculating cell update rates (purple) and updating states (red) are shown as color-coded flowcharts.

Algorithm 1 Agent-based model

Require: System parameters and cell state transition parameters
Ensure: Cell information matrix and population counts per type

Initialize: randomly distributed cells
for $t = 0$ **to** T_{end} **do**
  Select a random cell: $id \leftarrow \lfloor \text{rand}() \cdot CellNum \rfloor$
  Calculate transition rates:
  if No therapy **then**
    Calculate: $p^{id}_{dea}, p^{id}_{pro}, p^{id}_{mig}$ according to Eqs (2.1)–(2.11)
  else if Radiotherapy **then**
    Calculate: $p^{id}_{dea}, p^{id}_{pro}, p^{id}_{mig}$ according to Eq (2.12)
  else if Targeted therapy **then**
    if T_c **then**
      Update: x^t according to Eqs (2.14) and (2.15)
    end if
    Calculate: $p^{id}_{dea}, p^{id}_{pro}, p^{id}_{mig}$ according to Eq (2.13)
  else
    if T_c **then**
      Update: y^t according to Eq (2.17)
    end if
    Calculate: $p^{id}_{dea}, p^{id}_{pro}, p^{id}_{mig}$ according to Eq (2.16)
  end if
  Cell fate decision:
  Generate a random number: $r \leftarrow \text{rand}(0, 1)$
  if $r < p^{id}_{dea} \cdot \Delta t$ **then**
    Death: remove the cell
    $CellNum \leftarrow CellNum - 1$
  else if free neighboring space **then**
    if $r < (p^{id}_{dea} + p^{id}_{pro}) \cdot \Delta t$ **then**
      Proliferation: Daughter cells inherits H_{id}, x, y
      $CellNum \leftarrow CellNum + 1$
    else if $r < (p^{id}_{dea} + p^{id}_{pro} + p^{id}_{mig}) \cdot \Delta t$ **then**
      Migration: Update coordinates
    else
      Stationarity: No change in cell state
    end if
  else
    Stationarity: No change in cell state
  end if
  for $k = 1$ **to** n **do**
    Update: Information for the k-th neighbor cell
  end for
end for

2.2. *Agent-based model of tumor–immune interactions*

In this study, we investigate the interactions among tumor cells (C) and cytotoxic T cells (T_c), helper T cells (T_h), and regulatory T cells (T_r) (Figure 3). Specifically, in Figure 3, positive regulation is defined as enhancing the proliferation rate, whereas negative regulation increases the death rate. Intercellular interactions are primarily influenced by three factors.

(1) Cellular heterogeneity $\mathbf{H} = \{H_C, H_{T_c}, H_{T_h}, H_{T_r}\}$, which quantifies the phenotypic and functional diversity across cell types. $\mathbf{H}$ is specifically defined in Sections 2.2.1–2.2.4.
(2) The intercellular distance $\xi_{i,j}^k$ between Cell i and Cell j at the k-th neighbor position, which reflects the spatial influences on cellular behavior (Figure 1B).
(3) The neighboring sites n within the extended Moore neighborhood, describing the regulation of the local microenvironment (Figure 1B).

Additionally, we incorporate tumor drug resistance metrics $\mathbf{D} = \{x, y\}$ into the model to analyze tumors' evolutionary dynamics during treatment, providing a basis for optimizing treatment strategies. Here, x denotes the level of resistance to targeted therapy, and y denotes the level of resistance to immunotherapy, as described in Sections 2.3.2 and 2.3.3.

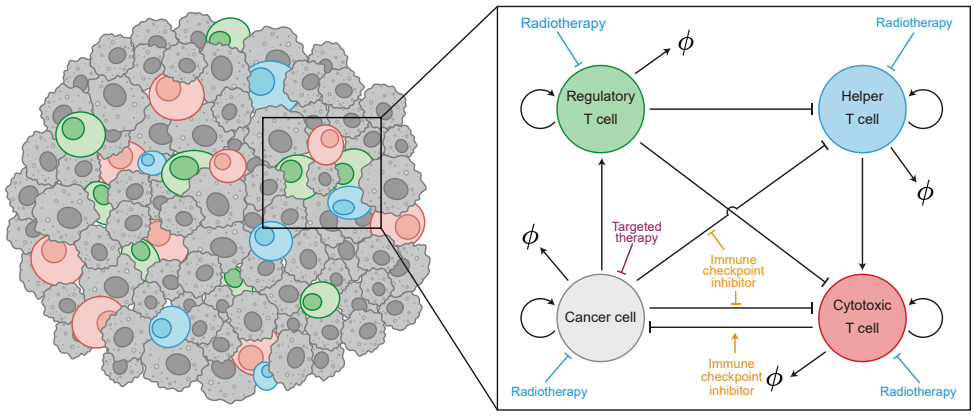

Figure 3. Mechanism diagram of tumor immune interactions. Tumor cells evade immune surveillance by inducing apoptosis in CTLs and Th cells, while simultaneously promoting the proliferation of Tregs. Tregs further suppress antitumor immunity by enhancing the death of CTLs and Th cells. Conversely, Th cells augment immune responses by stimulating CTLs' proliferation. CTLs serve as the primary effectors that directly eliminate tumor cells.

2.2.1. Computational framework for tumor cells

Tumor cells usually exhibit high heterogeneity and malignant proliferative potential [28–30]. To quantitatively characterize the heterogeneity among tumor cells, we introduce a metric $H_C \in [0, 1]$ that denotes their immunosuppressive potential, with an H_C approaching 1 indicating stronger immunosuppressive capacity, while an H_C near 0 reflects weaker immunosuppression. This metric provides a quantitative basis for analyzing tumor cell dynamics and tumor–immune interactions in the microenvironment.

Proliferation rate. We postulate that tumor cell proliferation depends exclusively on the cell itself

and is not influenced by the adjacent cells. Therefore, the proliferation rate of tumor cells p^C_{pro} is given by a constant $p^C_{pro,base}$.

Death rate. Within the TME, CTLs induce tumor cell lysis and apoptosis by releasing cytotoxic substances (e.g., perforin and granzymes) and secreting cytokines (e.g., IFN-γ) [31–33]. Therefore, depending on the interaction between tumor cells and CTLs (Figure 3), the death rate of tumor cells is defined as

$$p^C_{dea} = p^C_{dea,base} + p^C_{dea,T_c} \cdot \frac{1}{n}\left(\sum_{k=1}^{n} \delta_{k,T_c} \cdot \frac{1}{\xi^k_{C,T_c}} \cdot H^k_{T_c}\right), \tag{2.1}$$

where $p^C_{dea,base}$ denotes the baseline death rate of tumor cells, p^C_{dea,T_c} is the regulatory coefficient of tumor cell death mediated by CTLs, and $n = 48$ denotes the total number of neighboring positions within three layers surrounding the central cell, as illustrated in Figure 1B. Moreover, δ_{k,T_c} is the Dirac delta function indicating whether the k-th neighbor of the tumor cell is a CTL, and $H^k_{T_c}$ denotes the cytotoxic activity level of the CTL at that position (specifically defined in Section 2.2.2). The effectiveness of CTLs in killing tumor cells varies depending on their proximity and cytotoxicity: CTLs located closer to tumor cells and exhibiting higher cytotoxicity demonstrate enhanced killing effectiveness, whereas those further away with lower cytotoxicity are less effective.

Migration rate. The migration behavior of tumor cells is significantly regulated by the local microenvironmental density. Cells located at the tumor's periphery, surrounded by more empty spaces, are more prone to migrate outward to access resources and facilitate expansion. In contrast, cells within the tumor's interior, where the density is higher and the available space is limited, exhibit a correspondingly lower migration probability. Accordingly, the migration rate of tumor cells is defined as follows:

$$p^C_{mig} = p^C_{mig,base} + p^C_{mig,space} \cdot \frac{1}{n}\left(n - \sum_{k=1}^{n}\sum_{j=1}^{m} \delta_{k,j}\right), \tag{2.2}$$

where $p^C_{mig,base}$ denotes the baseline migration rate of tumor cells, $p^C_{mig,space}$ denotes the spatial-information-mediated regulatory coefficient for tumor cell migration, $(n - \sum_{k=1}^{n}\sum_{j=1}^{m} \delta_{k,j})$ denotes the number of empty agent sites around the current cell, and $m = 4$ corresponds to the four cell types considered in the model.

Stationary rate. According to the definition of "stationary" in Section 2.1, the stationary probability is denoted as

$$P^C_{sta} = 1 - (p^C_{dea} + p^C_{mig} + p^C_{pro}) \cdot \Delta t, \tag{2.3}$$

and thus the stationary rate is defined accordingly as follows:

$$p^C_{sta} = \frac{1}{\Delta t} - p^C_{dea} - p^C_{mig} - p^C_{pro}. \tag{2.4}$$

During the calculation process, we verified that the value of p_{sta} is non-negative across all cell types and treatment strategies. The subsequent calculation of the quiescence rate for immune cells follows a similar approach to that for tumor cells.

2.2.2. Computational framework for CTLs

As the key immune cells responsible for tumor recognition and elimination, CTLs exhibit functional heterogeneity primarily manifested in their cytotoxic levels [31–35]. We therefore introduce a heterogeneity metric $H_{T_c} \in [0, 1]$ that quantifies the cytotoxicity levels of CTLs. Higher H_{T_c} values indicate

stronger tumoricidal capacity, while lower values reflect diminished capacity. In tumor immunology, H_{T_c} can also represent the secretion levels of IFN-γ, granzymes, and perforin.

Proliferation rate. Within the TME, Th cells enhance CTLs' proliferation through Interleukin (IL)-2 secretion [36–38]. Thus, the proliferation rate of CTLs is defined as

$$p_{pro}^{T_c} = p_{pro,base}^{T_c} + p_{pro,T_h}^{T_c} \cdot \frac{1}{n}(\sum_{k=1}^{n} \delta_{k,T_h} \cdot \frac{1}{\xi_{T_c,T_h}^{k}} \cdot H_{T_h}^{k}), \tag{2.5}$$

where $p_{pro,base}^{T_c}$ denotes the baseline proliferation rate of CTLs, $p_{pro,T_h}^{T_c}$ denotes the Th cell-mediated regulatory coefficient for CTL proliferation, δ_{k,T_h} denotes whether the k-th neighboring position contains a Th cell, and $H_{T_h}^{k}$ quantifies the proproliferative capacity of the k-th Th cell's neighbor (specifically defined in Section 2.2.3). Higher H_{T_h} values indicate stronger proproliferative effects on CTLs, while lower values indicate weaker effects.

Death rate. Tumor cells promote CTL apoptosis by expressing PD-L1 molecules [39, 40]. Additionally, as an immunosuppressive T cell subpopulation, Tregs play a critical role in promoting CTL death [41–44]. Therefore, the death rate of CTLs is defined as

$$p_{dea}^{T_c} = p_{dea,base}^{T_c} + p_{dea,C}^{Tc} \cdot \frac{1}{n}(\sum_{k=1}^{n} \delta_{k,C} \cdot \frac{1}{\xi_{T_c,C}^{k}} \cdot H_{C}^{k}) + p_{dea,T_r}^{T_c} \cdot \frac{1}{n}(\sum_{k=1}^{n} \delta_{k,T_r} \cdot \frac{1}{\xi_{T_c,T_r}^{k}} \cdot H_{T_r}^{k}), \tag{2.6}$$

where $p_{dea,base}^{T_c}$ denotes the baseline death rate of CTLs, $p_{dea,C}^{T_c}$ denotes the death regulation coefficients mediated by tumor cells, $\delta_{k,C}$ denotes whether the k-th neighboring position contains a tumor cell, and H_{C}^{k} denotes the inhibitory levels of the tumor cell at that position. Higher values of H_{C}^{k} indicate stronger suppression of CTL by tumor cells. $H_{T_r}^{k}$ influences CTLs' mortality through mechanisms similar to H_{C}^{k}. The specific definition of $H_{T_r}^{k}$ is given in Section 2.2.4.

Migration rate. The migration rate of CTLs is defined as

$$p_{mig}^{T_c} = p_{mig,base}^{T_c} + p_{mig,space}^{T_c} \cdot \frac{1}{n}(n - \sum_{k=1}^{n}\sum_{j=1}^{m} \delta_{k,j}), \tag{2.7}$$

where $p_{mig,base}^{T_c}$ denotes the baseline migration rate of CTLs, and $p_{mig,space}^{T_c}$ denotes the space-mediated mirgation regulatory coefficient of CTLs.

2.2.3. Computational framework for helper T cells

The heterogeneity of Th cells is primarily characterized by their capacity to secrete IL-2, a cytokine that potently enhances CTLs' proliferation and activation [37, 45]. We define a heterogeneity metric $H_{T_h} \in [0, 1]$ to quantify the proproliferative capacity of Th cells toward CTLs.

Proliferation rate. The proliferation rate of Th cells $p_{pro}^{T_h}$ is given by a constant $p_{pro,base}^{T_h}$.

Death rate. Similar to their interaction with CTLs, both tumor cells and Tregs promote Th cell death [41–44]. Therefore, the death rate of Th cells is defined as

$$p_{dea}^{T_h} = p_{dea,base}^{T_h} + p_{dea,C}^{T_h} \cdot \frac{1}{n}(\sum_{k=1}^{n} \delta_{k,C} \cdot \frac{1}{\xi_{T_h,C}^{k}} \cdot H_{C}^{k}) + p_{dea,T_r}^{T_h} \cdot \frac{1}{n}(\sum_{k=1}^{n} \delta_{k,T_r} \cdot \frac{1}{\xi_{T_h,T_r}^{k}} \cdot H_{T_r}^{k}), \tag{2.8}$$

where $p^{T_h}_{dea,base}$ denotes the baseline death rate of Th cells, and $p^{T_h}_{dea,C}$ and $p^{T_h}_{dea,T_r}$ denote the death regulatory coefficient mediated by tumor cells and Tregs, respectively.

Migration rate. The migration rate of Th cells is defined as follows:

$$p^{T_h}_{mig} = p^{T_h}_{mig,base} + p^{T_h}_{mig,space} \cdot \frac{1}{n}(n - \sum_{k=1}^{n}\sum_{j=1}^{m}\delta_{k,j}), \tag{2.9}$$

where $p^{T_h}_{mig,base}$ denotes the baseline migration rate of Th cells, and $p^{T_h}_{mig,space}$ denotes the space-mediated regulatory coefficient for Th cell migration.

2.2.4. Computational framework for regulatory T cells

We introduce a Treg heterogeneity metric $H_{T_r} \in [0, 1]$ to quantify the immunosuppressive level of Tregs, where a higher H_{T_r} value indicates stronger immunosuppression. In tumor immunology, H_{T_r} can be interpreted as representing the secretion levels of IL-10 and tumor growth factor (TGF)-β by Tregs, which are known to play important roles in suppressing the differentiation and proliferation of both Th cells and CTLs [41–44].

Proliferation rate. In the TME, tumor cells shape the formation of an immunosuppressive microenvironment by recruiting and promoting the proliferation of Tregs [3, 46–48]. Therefore, the proliferation rate of Tregs is defined as

$$p^{T_r}_{pro} = p^{T_r}_{pro,base} + p^{T_r}_{pro,C} \cdot \frac{1}{n}(\sum_{k=1}^{n}\delta_{k,C} \cdot \frac{1}{\xi^k_{T_r,C}} \cdot H^k_C), \tag{2.10}$$

where $p^{T_r}_{pro,base}$ denotes the baseline proliferation rate of Tregs, and $p^{T_r}_{pro,C}$ denotes the tumor cell-mediated proliferation regulatory coefficient of Tregs.

Death rate. The death rate of Tregs $p^{T_r}_{dea}$ is given by a constant $p^{T_r}_{dea,base}$ without therapy stress.

Migration rate. The migration rate of Tregs is defined as

$$p^{T_r}_{mig} = p^{T_r}_{mig,base} + p^{T_r}_{mig,space} \cdot \frac{1}{n}(n - \sum_{k=1}^{n}\sum_{j=1}^{m}\delta_{k,j}), \tag{2.11}$$

where $p^{T_r}_{mig,base}$ denotes the baseline migration rate of Tregs, and $p^{T_r}_{mig,space}$ denotes the space-mediated migration regulatory coefficient of Tregs.

2.3. The ABM under different treatment options

To comparatively analyze treatment effects on immune response dynamics and therapeutic outcomes during tumor evolution, we implemented three treatment regimens.

(1) **Radiotherapy** preferentially kills rapidly dividing cells with impaired DNA repair capacity [49,50]. Because tumor cells generally have a higher rate of proliferation and a weaker ability to repair DNA than normal cells, they are more likely to die after radiotherapy [51, 52].
(2) **Targeted therapy** achieves selective tumor cell killing by specifically binding to oncogenic sites on tumor cells while sparing normal cells [53, 54].

(3) **Immunotherapy** eliminates tumor cells through immune checkpoint inhibitors (ICIs). In the TME, PD-L1-expressing tumor cells engage PD-1 receptors on T cells to suppress T cell proliferation and impair antitumor immunity, enabling immune escape. PD-1/PD-L1 inhibitors counteract this immune evasion by blocking the PD-1/PD-L1 signaling pathway, thereby reactivating T cells' function and enhancing tumor cell killing [40, 55].

2.3.1. Radiotherapy

We hypothesize that radiotherapy increases the death of all cells (Figure 3), but its effect on tumor cell death is significantly higher than that on immune cells, thereby achieving effective tumor killing. After applying radiotherapy, the death rates of various cell types are described as follows:

$$\begin{aligned}
p_{dea}^{C} &= p_{dea,base}^{C} + p_{dea,T_c}^{C} \cdot \frac{1}{n}\Big(\sum_{k=1}^{n} \delta_{k,T_c} \cdot \frac{1}{\xi_{C,T_c}^{k}} \cdot H_{T_c}^{k}\Big) + p_{dea,rad}^{C}, \\
p_{dea}^{T_c} &= p_{dea,base}^{T_c} + p_{dea,C}^{T_c} \cdot \frac{1}{n}\Big(\sum_{k=1}^{n} \delta_{k,C} \cdot \frac{1}{\xi_{T_c,C}^{k}} \cdot H_{C}^{k}\Big) \\
&\quad + p_{dea,T_r}^{T_c} \cdot \frac{1}{n}\Big(\sum_{k=1}^{n} \delta_{k,T_r} \cdot \frac{1}{\xi_{T_c,T_r}^{k}} \cdot H_{T_r}^{k}\Big) + p_{dea,rad}^{T_c}, \\
p_{dea}^{T_h} &= p_{dea,base}^{T_h} + p_{dea,C}^{T_h} \cdot \frac{1}{n}\Big(\sum_{k=1}^{n} \delta_{k,C} \cdot \frac{1}{\xi_{T_h,C}^{k}} \cdot H_{C}^{k}\Big) \\
&\quad + p_{dea,T_r}^{T_h} \cdot \frac{1}{n}\Big(\sum_{k=1}^{n} \delta_{k,T_r} \cdot \frac{1}{\xi_{T_h,T_r}^{k}} \cdot H_{T_r}^{k}\Big) + p_{dea,rad}^{T_h}, \\
p_{dea}^{T_r} &= p_{dea,base}^{T_r} + p_{dea,rad}^{T_r},
\end{aligned} \tag{2.12}$$

where $p_{dea,rad}^{C}$, $p_{dea,rad}^{T_c}$, $p_{dea,rad}^{T_h}$, and $p_{dea,rad}^{T_r}$, respectively, denote the killing efficacy of radiotherapy on tumor cells, CTLs, Th cells, and Tregs. When simulating the dynamic evolution of the tumor under radiotherapy, Eqs (2.1), (2.6), and (2.8) are replaced by Eq (2.12).

2.3.2. Targeted therapy

We hypothesize that targeted drugs significantly increase the death rate of tumor cells without affecting other cells. Meanwhile, tumor cells exhibit heterogeneity in their response to targeted drugs, and treatment-induced phenotypic adaptation may lead to drug resistance [56,57]. Hence, we introduce a drug resistance metric $x \in [0, 1]$ for tumor cells to characterize the dynamic evolution of drug resistance during targeted therapy and its impact on treatment efficacy. Consequently, the death rate of tumor cells under targeted therapy is defined as

$$p_{dea}^{C} = p_{dea,base}^{C} + p_{dea,T_c}^{C} \cdot \frac{1}{n}\Big(\sum_{k=1}^{n} \delta_{k,T_c} \cdot \frac{1}{\xi_{C,T_c}^{k}} \cdot H_{T_c}^{k}\Big) + p_{dea,tar}^{C} \frac{{x_0}^{n_1}}{{x_0}^{n_1} + x^{n_1}}, \tag{2.13}$$

where $p_{dea,tar}^{C}$ denotes the regulatory coefficient for targeted drug-induced tumor cell apoptosis, x denotes the drug resistance metric, x_0 is the half-saturation constant of drug resistance, and n_1 denotes the Hill coefficient. As resistance increases, therapeutic efficacy gradually diminishes. In the simulations, Eq

(2.13) replaces Eq (2.1) to better capture the resistance effects. In the current model, for simplicity, the concentration of targeted drugs is assumed to be spatially uniform, and any potential effects of drug diffusion or heterogeneous vascular distribution are not considered.

The tumor cell resistance may undergo random changes due to phenotypic variation. For simplicity, we assume that the dynamic update of the resistance metric x follows a Markov process. The value at Step t, x^t, is updated to x^{t+1} according to a transition probability conditioned on x^t. To maintain the range $0 \leq x \leq 1$, we adopt a conditional beta distribution

$$P(x^{t+1} = x|x^t) \sim B(x|a, b) = \frac{\Gamma(a+b)}{\Gamma(a)\Gamma(b)} x^{a-1}(1-x)^{b-1}, \tag{2.14}$$

with the shape parameters

$$a = x^t\eta_1, b = (1-x^t)\eta_1, \tag{2.15}$$

where η_1 quantifies the drug resistance update rate. It should be noted that a larger value of η indicates weaker development of resistance (i.e., smaller variance in the resistance metric update). This choice ensures that the conditional expectation and variance are

$$\mathrm{E}(x^{t+1}|x^t) = x^t, \mathrm{Var}(x^{t+1}|x^t) = \frac{1}{1+\eta_1} x^t(1-x^t).$$

The initial values of x are randomly sampled from $[0, 1]$ before treatment, and the resistance metrics are updated at each time step after treatment.

It should be noted that the resistance metric $x \in [0, 1]$ is a normalized relative index representing the degree of drug tolerance of an individual tumor cell, rather than a pharmacological variable such as drug concentration. By introducing a half-saturation constant x_0, the Hill function $\frac{x_0^{n_1}}{x_0^{n_1}+x^{n_1}}$ approaches zero as $x \to 1$, effectively capturing the loss of drug efficacy under complete resistance. Regarding the origin of resistance, the model assumes the pre-existence of subpopulations with varying resistance levels (the initial x values are randomly sampled from $[0, 1]$), reflecting intratumoral heterogeneity. During treatment, the resistance metric evolves stochastically via a Markov process, allowing both increases and decreases to model the dynamic gain and loss of drug resistance. This formulation enables the model to span the full phenotypic spectrum from sensitive to resistant states within a bounded interval.

2.3.3. Immunotherapy

For immunotherapy, we assume that PD-1/PD-L1 inhibitors function in two ways (Figure 3): Directly enhancing the killing capacity of CTLs against tumor cells, and reducing tumor cell-mediated immunosuppression of CTLs and Th cells by blocking the PD-1/PD-L1 pathway. Accordingly, the

death rates of tumor cells, CTLs, and Th cells during immunotherapy are defined as follows:

$$
\begin{aligned}
p_{dea}^{C} &= p_{dea,base}^{C} + p_{dea,T_c}^{C} \cdot \frac{1}{n}\Big(\sum_{k=1}^{n} \delta_{k,T_c} \cdot \frac{1}{\xi_{C,T_c}^{k}} \cdot H_{T_c}^{k}\Big) \cdot \Big(1 + p_{dea,ICI}^{C} \frac{{y_0}^{n_2}}{{y_0}^{n_2} + y^{n_2}}\Big), \\
p_{dea}^{T_c} &= p_{dea,base}^{T_c} + p_{dea,C}^{T_c} \cdot \frac{1}{n}\Big(\sum_{k=1}^{n} \delta_{k,C} \cdot \frac{1}{\xi_{T_c,C}^{k}} \cdot H_{C}^{k}\Big) \cdot \Big(1 + p_{dea,ICI}^{T_c} \frac{{y_k}^{n_2}}{{y_k}^{n_2} + {y_0}^{n_2}}\Big) \\
&\quad + p_{dea,T_r}^{T_c} \cdot \frac{1}{n}\Big(\sum_{k=1}^{n} \delta_{k,T_r} \cdot \frac{1}{\xi_{T_c,T_r}^{k}} \cdot H_{T_r}^{k}\Big), \\
p_{dea}^{T_h} &= p_{dea,base}^{T_h} + p_{dea,C}^{T_h} \cdot \frac{1}{n}\Big(\sum_{k=1}^{n} \delta_{k,C} \cdot \frac{1}{\xi_{T_h,C}^{k}} \cdot H_{C}^{k}\Big) \cdot \Big(1 + p_{dea,ICI}^{T_h} \frac{{y_k}^{n_2}}{{y_k}^{n_2} + {y_0}^{n_2}}\Big) \\
&\quad + p_{dea,T_r}^{T_h} \cdot \frac{1}{n}\Big(\sum_{k=1}^{n} \delta_{k,T_r} \cdot \frac{1}{\xi_{T_h,T_r}^{k}} \cdot H_{T_r}^{k}\Big),
\end{aligned}
\tag{2.16}
$$

where $p_{dea,ICI}^{C}$, $p_{dea,ICI}^{T_c}$, and $p_{dea,ICI}^{T_h}$ denote the regulatory coefficients of ICI treatment on tumor cells, CTLs, and Th cells, respectively. Here, y is the ICI resistance metric for tumor cells, and y_k is the resistance level of the k-th tumor cell adjacent to CTLs or Th cells. The parameter y_0 denotes the half-saturation constant, and n_2 is the Hill coefficient. In the simulations, Eq (2.16) replaces Eqs (2.1), (2.6), and (2.8) to represent the effect of immunotherapy.

Similar to resistance to targeted therapy, we model the resistance dynamics for immunotherapy using a conditional beta distribution

$$
P(y^{t+1} = y | y^t) \sim B(y|a, b) \tag{2.17}
$$

with the shape parameters

$$
a = y^t \eta_2, b = (1 - y^t)\eta_2.
$$

Thus, the conditional expectation and variance of y^{t+1} are

$$
E(y^{t+1}|y^t) = y^t, \mathrm{Var}(y^{t+1}|y^t) = \frac{1}{1 + \eta_2} y^t (1 - y^t).
$$

The initial values of y are randomly sampled from the interval $[0, 1]$, and the resistance metrics are updated at each time step following treatment. The range of y is defined analogously to that of x in the previous section.

2.4. Model parameters

All key parameters used in the model simulation are listed in Table 1. The total simulation time T_{end}, the time step Δt, the spatial dimensions, and the initial cell counts are kept fixed as basic parameters. To realistically reflect the clinical TME, the initial fractions of different cell types are chosen within ranges according to the cellular composition observed in cancer patients. The initial cell numbers are randomly sampled from these ranges. Other parameters, including cell transition rates and regulation coefficients, are configured according to specific treatment scenarios.

The current study was intended to develop an ABM, instead of simulating a real tumor's evolution dynamics. Therefore, parameterization and calibration focus on providing a qualitative, mechanistic

representation for typical tumor evolution dynamics in mice. For example, tumor cells rapidly expand in 10 days without immunosuppression, as well as the rational ratios of immune cell subpopulations (immune cell populations referred to https://isb-cgc.shinyapps.io/shiny-iatlas/).

Table 1. Agent-based model parameter values.

Parameter	Value	Unit*	Description
SpaceWidth	100	-	Width of the two-dimensional space
SpaceLength	100	-	Length of the two-dimensional space
T_{end}	60	day	Total simulation time
Δt	0.001	day	Simulation time step
$N_{C,ini}$	[580, 620]	-	Initial number of tumor cells
$N_{T_c,ini}$	[160, 180]	-	Initial number of cytotoxic T cells
$N_{T_r,ini}$	[40, 60]	-	Initial number of regulatory T cells
$N_{T_h,ini}$	[190, 210]	-	Initial number of helper T cells
n	48	-	Number of neighboring agents (3 concentric layers)
$p^C_{dea,base}$	10.00	1/day	Baseline death rate of tumor cells (C)
$p^C_{pro,base}$	250.00	1/day	Baseline proliferation rate of C
$p^C_{mig,base}$	100.00	1/day	Baseline migration rate of C
$p^C_{mig,space}$	100.00	1/day	Spatially mediated regulatory coefficient of C migration
p^C_{dea,T_c}	10, 500.00	1/day	T_c-mediated regulation coefficient of C death
$p^C_{dea,rad}$	200.00	1/day	Radiotherapy-induced death rate increase for C
$p^C_{dea,tar}$	600.00	1/day	Targeted therapy-induced death rate increase for C
x_0	0.5	-	Half-saturation constant for targeted therapy resistance
n_1	2	-	Hill coefficient for targeted therapy resistance
η_1	100	-	Resistance update parameter (targeted therapy)
$p^C_{dea,ICI}$	26, 000.00	1/day	Immunotherapy-induced death rate increase for C
y_0	0.5	-	Half-saturation constant for ICI resistance
n_2	6	-	Hill coefficient for ICI resistance
η_2	100	-	Resistance update parameter (immunotherapy)
$p^{T_c}_{dea,base}$	30.00	1/day	Baseline death rate of CTLs (T_c)
$p^{T_c}_{pro,base}$	150.00	1/day	Baseline proliferation rate of T_c
$p^{T_c}_{mig,base}$	600.00	1/day	Baseline migration rate of T_c
$p^{T_c}_{mig,space}$	600.00	1/day	Spatially mediated regulatory coefficient of T_c migration
$p^{T_c}_{dea,C}$	10, 500.00	1/day	C-mediated regulation coefficient of T_c death
$p^{T_c}_{dea,T_r}$	8700.00	1/day	T_r-mediated regulation coefficient of T_c death
$p^{T_c}_{pro,T_h}$	10, 600.00	1/day	T_h-mediated regulation coefficient of T_c proliferation
$p^{T_c}_{dea,rad}$	150.00	1/day	Radiotherapy-induced death rate increase for T_c
$p^{T_c}_{dea,ICI}$	10.00	1/day	Immunotherapy-induced death rate increase for T_c
$p^{T_h}_{dea,base}$	30.00	1/day	Baseline death rate of Th cells (T_h)
$p^{T_h}_{pro,base}$	150.00	1/day	Baseline proliferation rate of T_h
$p^{T_h}_{mig,base}$	550.00	1/day	Baseline migration rate of T_h

Continued on next page

Parameter	Value	Unit*	Description
$p^{T_h}_{mig,space}$	600.00	1/day	Spatial mediated regulatory coefficient of T_h migration
$p^{T_h}_{dea,C}$	8900.00	1/day	C-mediated regulation coefficient of T_h death
$p^{T_h}_{dea,T_r}$	8700.00	1/day	T_r-mediated regulation coefficient of T_h death
$p^{T_h}_{dea,rad}$	150.00	1/day	Radiotherapy-induced death rate increase for T_h
$p^{T_h}_{dea,ICI}$	10.00	1/day	Immunotherapy-induced death rate increase for T_h
$p^{T_r}_{dea,base}$	30.00	1/day	Baseline death rate of Treg cells (T_r)
$p^{T_r}_{pro,base}$	50.00	1/day	Baseline proliferation rate of T_r
$p^{T_r}_{mig,base}$	700.00	1/day	Baseline migration rate of T_r
$p^{T_r}_{mig,space}$	600.00	1/day	Spatial mediated regulatory coefficient of T_r migration
$p^{T_r}_{pro,C}$	8700.00	1/day	C-mediated regulation coefficient of T_r proliferation
$p^{T_r}_{dea,rad}$	200.00	1/day	Radiotherapy-induced death rate increase for T_r

*Note: The state transition rates correspond to the rate of a single cell in each cell fate decision. For example, since only one cell is sampled in each step, the rate constants $p^C_{dea,base}$ and p^C_{dea,T_c} may not directly correspond to the death rate of tumor cells. In simulations, we set $p^C_{dea,base}$ and p^C_{dea,T_c}, so that the average probability of a tumor cell dying per time step is about 0.1 without therapy (Figure 4A), corresponding to a death rate of ≈ 0.1 day^{-1}, given a time step $\Delta t = 10^{-3}$ day and approximately 10^3–10^4 cells.

3. Results

3.1. Stochastic simulation of tumor–immune interactions

To investigate the impact of the immune system on tumor growth, we first simulate the spatiotemporal dynamics of tumor growth under untreated conditions on the basis of Eqs (2.1)–(2.11). To ensure the reliability of the simulation results, we perform 100 independent stochastic simulations. Figure 4 shows the temporal trends of different cell populations across the 100 simulations, along with the spatial distribution characteristics at different time points.

The simulation results show that tumor cell numbers increase rapidly at Time 0, then gradually stabilize (Figure 4A). This trend may be attributed to the sparse initial cell distribution and limited immune cell infiltration during early tumor development, which collectively create favorable conditions for rapid proliferation. The eventual stabilization of tumor cell numbers occurs as cells gradually fill the predefined circular spatial domain over time. To better approximate the morphological characteristics of solid tumors, we set a maximum radial expansion limit in the model, restricting cell proliferation and migration within this finite space. Concurrently, CTL numbers rise significantly during the first 20 days before gradually declining. Treg populations continuously increase in the TME, while Th cell numbers slowly decrease (Figure 4A). The ratio of CTLs to tumor cells, which reflects the immune killing capacity in the TME, exhibits a dynamic trend of an initial increase followed by a decline (Figure 4B).

These results demonstrate the complex interactions between immune cells' dynamics and the tumor growth in the TME. The initial increase in CTLs reflects the immune system's early response to the tumor's presence, while the subsequent decline reveals immunosuppressive effects and spatial competition triggered by tumor cells and Tregs. The continuous rise in Tregs further exacerbates the formation of an immunosuppressive microenvironment, limiting the function of CTLs and Th cells. The gradual decrease in Th cells can be attributed to immunosuppression induced by both tumor cells

and Tregs. The changes in immune killing capacity in the microenvironment illustrate spontaneous evolution toward an immunosuppressive state in the absence of therapeutic intervention. Overall, these dynamic changes revealed key mechanisms of tumors' immune evasion and provided important insights into the complexity of tumor–immune interactions.

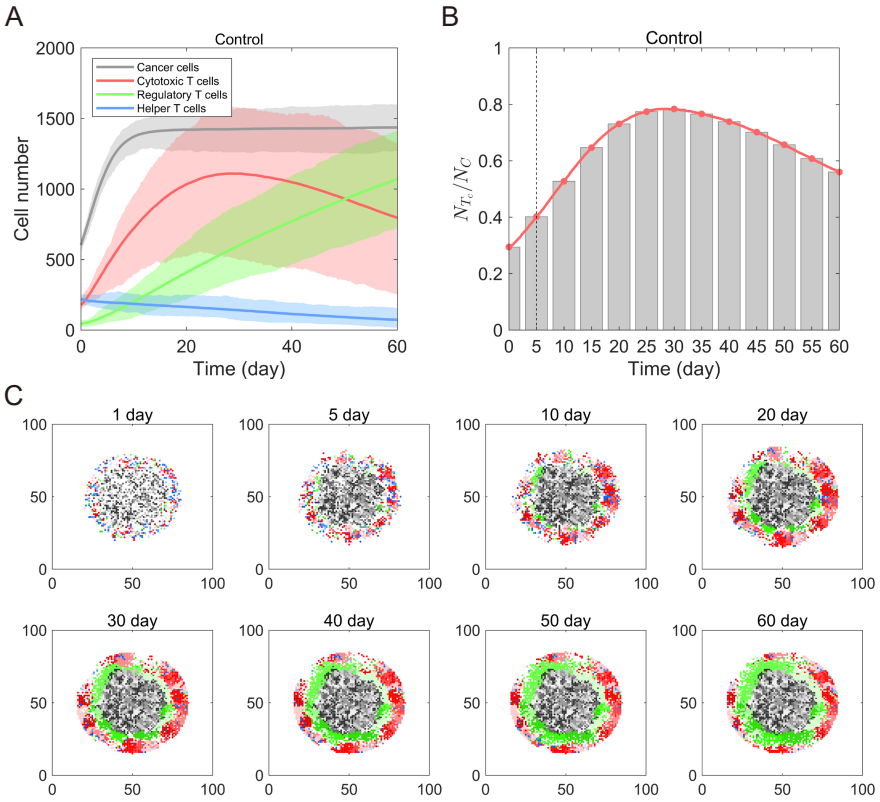

Figure 4. Simulation of tumors' evolution under tumor–immune cell interactions. (A) Cell population dynamics over 60 days, with the shaded regions showing the ranges of 100 stochastic simulations and the solid lines indicating their mean values. (B) The ratio of CTLs to tumor cells over time. (C) Two-dimensional spatial distributions recorded every 5 days: Gray dots for tumor cells, red dots for CTLs, green dots for Tregs, and blue dots for Th cells. For cells of the same type, the shade of each dot indicates the value of the heterogeneity metric **H**: Darker shades represent higher **H** values, and lighter shades represent lower **H** values.

Additionally, from a spatial distribution perspective, immune cells are uniformly distributed at the tumor periphery during the first 5 days (Figure 4C). Subsequently, from Day 10 to Day 20, immune cells gradually migrated toward the tumor's region but did not infiltrate into the tumor's core. Instead, they accumulated at the edge of the tumor, forming a typical "immune desert" spatial pattern. Furthermore, between Days 30 and 60, Tregs form a ring-like "barrier" around the tumor's periphery, physically separating tumor cells from CTLs and thereby attenuating CTLs' tumoricidal effects (Figure 4C). In tumor immunology, this phenomenon is termed "immune privilege" [48], representing one of the key mechanisms of tumors' immune evasion. It should be noted that although the Treg-enclosing structure facilitates the tumor's immune escape, its spatial barrier effect also partially restricts outward tumor

expansion. It should be noted that, in the spatial distribution figures, cells of the same type are depicted using varying shades within the same color palette to represent differences in their heterogeneity, as quantified by the **H** value. Darker shades correspond to higher **H** values, while lighter shades indicate lower **H** values.

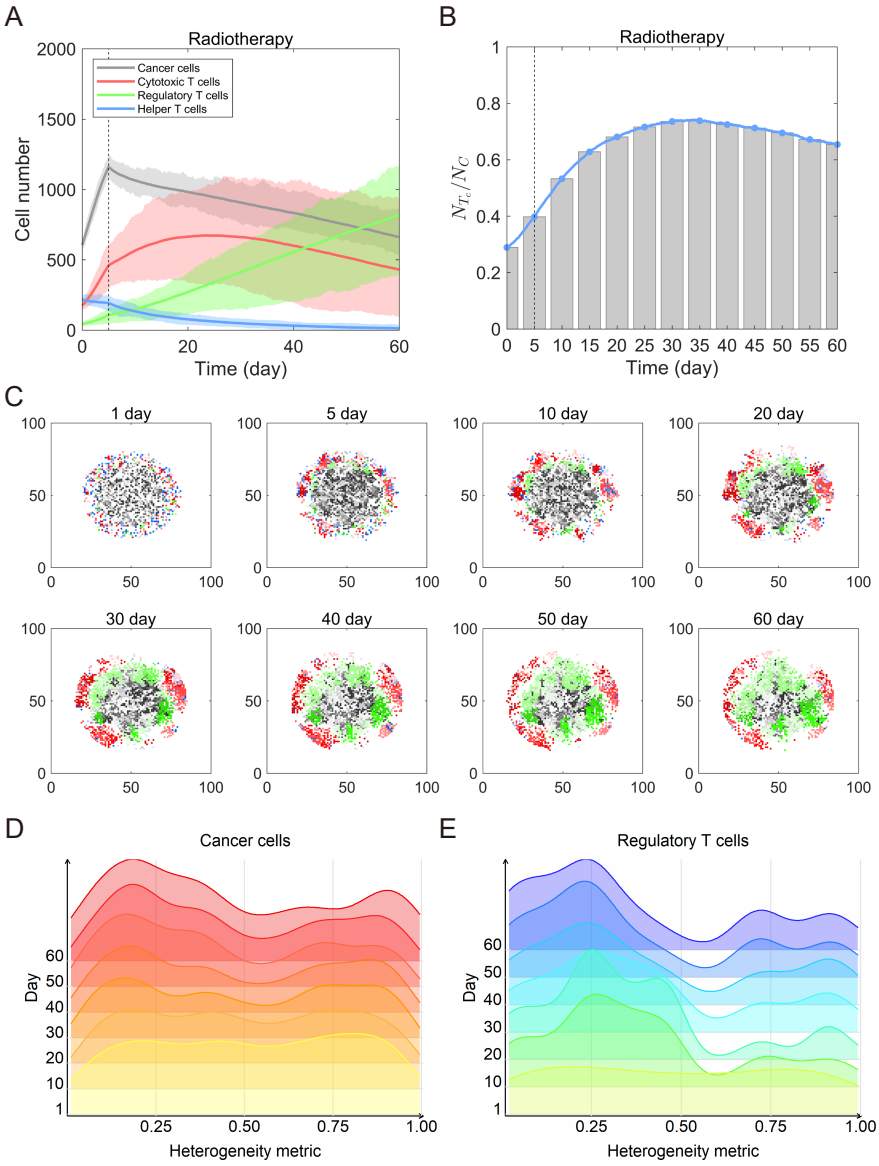

Figure 5. A simulated tumor–immune system's dynamics under radiotherapy. (A) Radiotherapy is administered from Day 5 to Day 60 on top of the baseline simulation. Solid lines show averaged cell population changes across 100 stochastic simulations. (B) Change in the ratio of CTLs to the number of tumor cells over time under radiotherapy. (C) The tumor–immune system's spatial distributions at different time points. Darker shades represent higher **H** values, and lighter shades represent lower **H** values. (D) Probability distribution of tumor cells' heterogeneity metrics over time. (E) Probability distribution of Tregs' heterogeneity metrics over time.

3.2. Tumor progression under different treatment methods

3.2.1. Radiotherapy

To elucidate the tumor–immune system's dynamics and therapeutic effects during radiotherapy, we apply Eq (2.12) for the cell death rates. The simulation results show that after radiotherapy is initiated on Day 5, tumor growth is significantly suppressed, with rapid tumor cell depletion. By Day 60, tumor cell counts decrease by approximately 50% compared with the baseline simulations (Figure 5A). During treatment, the counts of all immune cell populations also decreased relative to the baseline, whereas the killing capacity of T cells rapidly increased after the start of therapy, then slightly declined, ultimately stabilizing at approximately 0.65 (Figure 5B and Table 2). Comparison with the baseline simulations reveals that although radiotherapy damages immune cells to some extent, it ultimately enhances immune killing capacity and improves the TME in the later stages of the simulation.

From a spatial perspective, starting from Day 30, the effects of radiotherapy became evident, manifested by inhibited tumor volume expansion followed by gradual shrinkage, with significantly reduced cell density in the central regions in particular and loosened tumor tissue (Figure 5C). Meanwhile, Tregs remain distributed at the tumor's periphery, but their encirclement becomes less compact, providing increased opportunities for CTL infiltration. With continued radiotherapy, both tumor cells and Tregs display progressively lighter coloration, indicating substantial phenotypic alterations (Figure 5C–E). This observation suggests that radiotherapy, through selective pressure, may have preferentially preserved subpopulations with weaker immunosuppressive capacity, thereby modifying the immunosuppressive properties of the TME.

3.2.2. Targeted therapy

To investigate the dynamic changes in the tumor–immune system under targeted therapy, we use Eq (2.13) to describe the tumor cell death rate. Under targeted drug therapy, the tumor cell death rate significantly increases, and the therapeutic efficacy is simultaneously modulated by drug resistance.

The model's simulations show that after targeted therapy initiation, the tumor cell population decreases rapidly, reaching approximately 60% of its initial value by the end of the simulation, indicating significant antitumor efficacy (Figure 6A). Compared with the untreated group, targeted therapy leads to a notable increase in CTLs and Tregs, with a slight rise in Th cells (Figure 6A). This increase, however, does not represent genuinely unbounded growth. In our model, cell proliferation is strictly constrained by spatial availability. As tumor cells are substantially eliminated by targeted drugs, the space originally occupied by tumor cells is vacated, providing physical room for immune cells' expansion. Meanwhile, targeted drugs specifically kill tumor cells without directly affecting immune cells, allowing immune cells to survive and expand under therapeutic pressure. This simulation outcome is consistent with observations from preclinical studies. Previous research has shown that certain targeted therapies, such as B-Raf proto-oncogene, serine/threonine kinase (BRAF) inhibitors in melanoma, not only directly suppress tumor growth but also indirectly enhance antitumor immune responses by inducing immunogenic cell death and remodeling the TME, including increasing the number of tumor–infiltrating lymphocytes.

Following treatment initiation, the immune killing capacity in the TME shows significantly accelerated growth (Figure 6B). Up to Day 30, the rate of increase slows due to reduced CTL numbers. Nevertheless, the immune killing capacity maintains an upward trend, ultimately reaching a peak level of

2.65 at the end of the simulation. The spatial distribution of the tumor–immune system reveals that from Day 20 onward, tumor volume decreases significantly, and tumor cells become more sparsely distributed (Figure 6C). These results demonstrate that targeted therapy not only inhibits tumor growth but also enhances immune activity by remodeling the TME, offering new perspectives for cancer treatment.

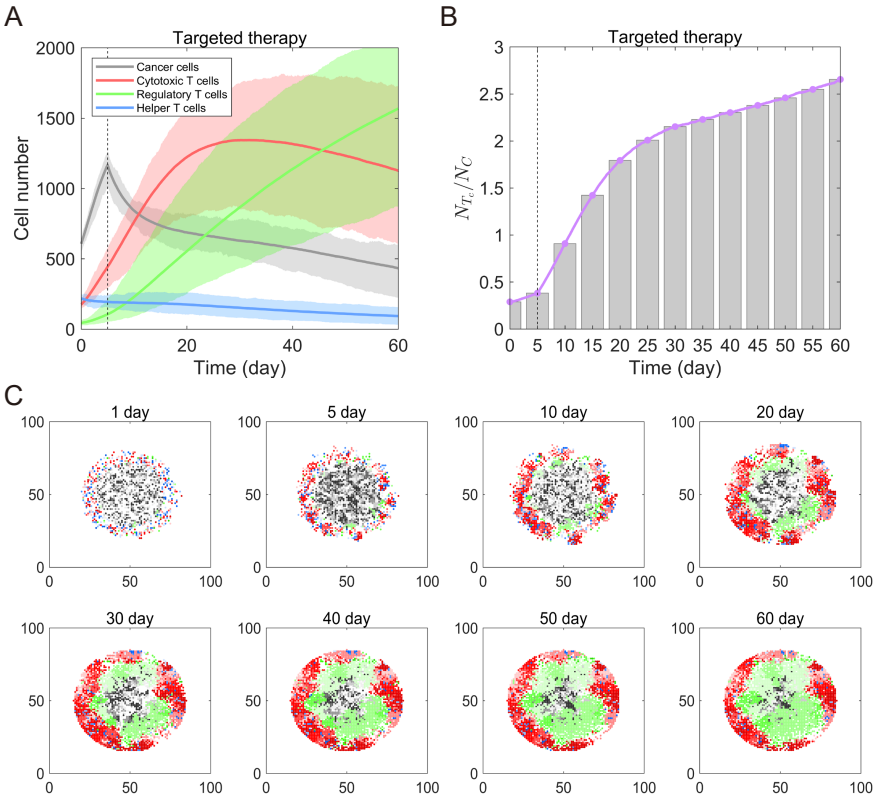

Figure 6. Simulation of tumor–immune system dynamics under targeted therapy. (A) The cell population changes from Day 5 to Day 60 with targeted therapy on top of the baseline simulation. Solid lines show the mean values from 100 stochastic simulations. (B) CTL to tumor cell number ratio changes over time. (C) Two-dimensional spatial distributions of the tumor–immune system at selected timepoints. Darker shades represent higher **H** values, and lighter shades represent lower **H** values.

3.2.3. Immunotherapy

Immune checkpoint inhibitors exert their therapeutic effects by enhancing the tumor-killing capacity of CTLs and suppressing tumors' immune evasion. In simulations, Eq (2.16) was used to describe the death rates of tumor cells, CTLs, and Th cells, simulating the therapeutic effects of PD-1/PD-L1 inhibitors.

Stochastic simulation results demonstrate that immunotherapy effectively suppresses tumor growth, as evidenced by a gradual decline in tumor cell numbers (Figure 7A). CTL counts increase rapidly during the initial treatment phase, then decrease slightly, yet ultimately remain higher than tumor cell counts. Although Treg numbers show slow but steady growth, they remain consistently lower than CTL counts. Th cell numbers stabilize after a transient increase. The CTL to tumor cell ratio shows

significant improvement, peaking at 1.24 around Day 35 and maintaining high levels until the treatment's termination (Figure 7B). These results indicate that ICIs not only effectively control tumor progression but also enhance the proliferation of CTLs with potent tumor-killing functions.

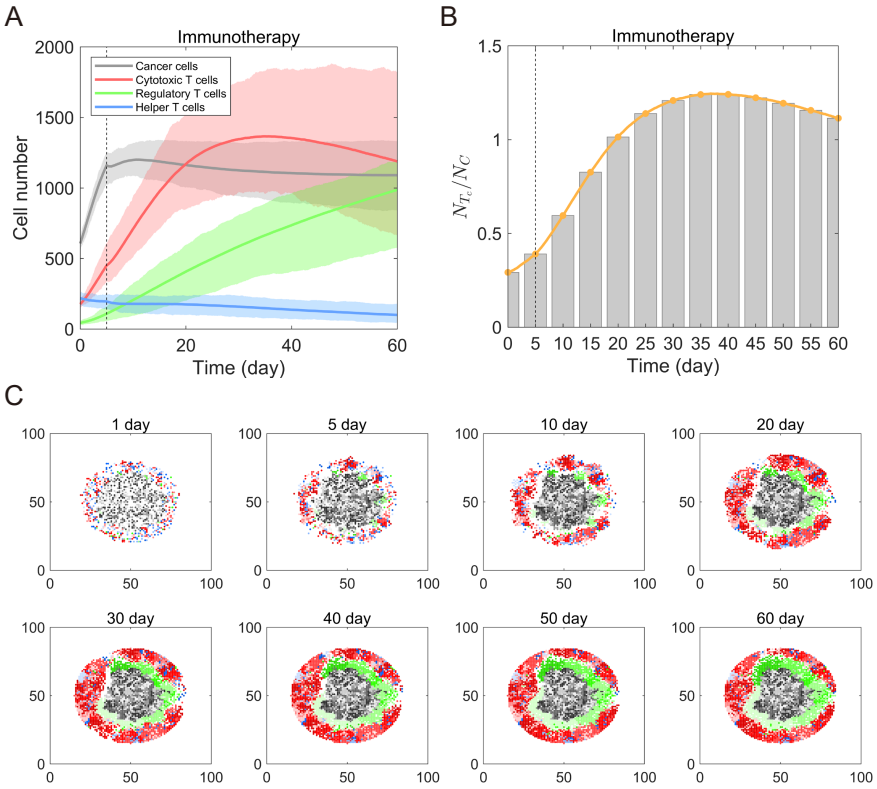

Figure 7. Simulated tumor–immune system's dynamics under immunotherapy. (A) The cell population changes from Day 5, when ICI treatment begin, until Day 60, when the simulation ended. Solid lines show averages of 100 simulations. (B) Changes in the ratio of CTLs to tumor cells over time under immunotherapy. (C) Two-dimensional spatial distributions of the tumor–immune system at selected time points. Darker shades represent higher **H** values, and lighter shades represent lower **H** values.

Spatially, the tumor volume stabilizes after approximately 15 days of treatment, halting further expansion (Figure 7C). This phenomenon may result from ICIs restoring T cell function and enhancing antitumor activity via PD-1/PD-L1 blockade. By the middle to late stages of the simulation, most CTLs appear dark red, while Th cells display dark blue coloration (Figure 7C). These results indicate that immunotherapy not only reduces the mortality of immune cells but also enhances functional diversity through increased heterogeneity. Specifically, dark red CTLs represent subpopulations with high cytotoxicity, while dark blue Th cells denote subpopulations with elevated IL-2 secretion capacity. This enhanced heterogeneity further optimizes immune responses within the TME, thereby strengthening antitumor immunity.

Notably, during the middle to late stages of immunotherapy, CTLs formed an encapsulating outer ring structure around the tumor's periphery (Figure 7C). This spatial pattern arises as follows: ICIs restore CTLs' cytotoxic function, enabling them to accumulate effectively at the tumor's margin. However,

the physical barriers formed by Tregs within the TME partially impede deep CTL infiltration into the tumor's core. Specifically, the ring-like Treg structure surrounding the tumor's periphery, termed immune privilege in Figure 4C, restricts CTLs' accumulation at the tumor's periphery. Joyce and Fearon systematically reviewed this phenomenon, noting that Tregs, cancer-associated fibroblasts, and aberrant vascular structures collectively form barriers that limit effector T cells' infiltration [48]. Thus, the encapsulating outer ring structure of CTLs observed in our model recapitulates this clinically relevant immune exclusion phenomenon, further validating the model's capability to capture spatial tumor–immune interactions.

3.3. Dynamics of drug resistance under different treatment options

To thoroughly analyze the dynamic changes in tumor cells during the progression of drug resistance under targeted therapy and immunotherapy, we introduced two drug resistance metrics: targeted therapy resistance x and immunotherapy resistance y. Here, we examine the changes in the resistance metrics after the start of therapy.

Simulation results show that on Day 1 without treatment, the tumor cell resistance metric follows a uniform distribution in $(0, 1)$. After initiating treatment on Day 5, the peak of the resistance metric's distribution gradually shifts rightward (Figure 8). This indicates that under drug selection pressure, most tumor cells develop increasing resistance, with the population evolving toward drug-resistant phenotypes. A comparison between Figure 8A (targeted therapy) and Figure 8B (immunotherapy) reveals more pronounced resistance evolution under targeted therapy. After targeted therapy, nearly no low-resistance subpopulations remain. In contrast, immunotherapy maintains drug-sensitive subpopulations throughout the simulation. These results suggest that tumor cells are more sensitive to targeted therapy, likely due to its direct action on specific molecular targets, which exerts stronger selection pressure. Conversely, immunotherapy indirectly eliminates tumor cells through immune activation, applying a weaker selection pressure that permits the persistence of sensitive subpopulations.

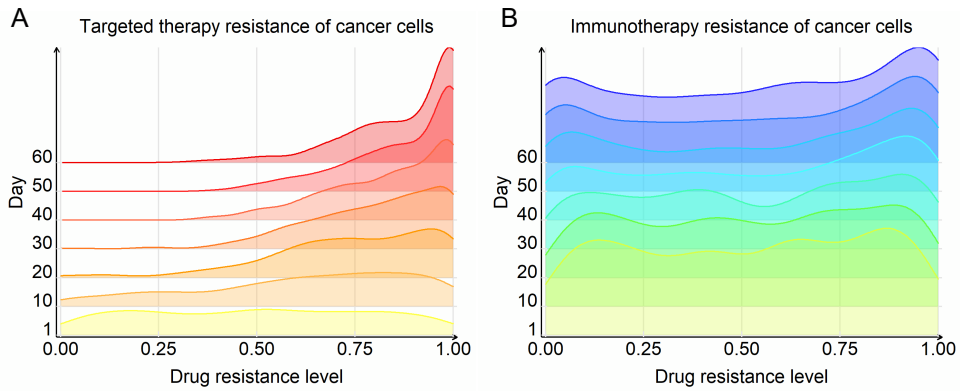

Figure 8. Dynamic changes in tumor cells' drug resistance during targeted therapy and immunotherapy. The probability distribution of drug resistance metrics across all tumor cells is calculated every 10 days. (A) Distribution under targeted therapy. (B) Distribution under immunotherapy.

Our findings from the model simulations provide key insights into how tumors develop drug resistance under various treatment strategies. They also lay the theoretical groundwork for optimizing

combination therapies. For instance, combining targeted therapy with immunotherapy may effectively postpone the onset of drug resistance. Targeted therapy works by directly eliminating tumor cells, while immunotherapy boosts the immune system's ability to remove any remaining resistant cells. Moreover, for subpopulations of tumors with lower drug resistance, more tailored treatment strategies can be developed. For example, single-cell sequencing technology can identify the characteristics of drug-sensitive cells, which can guide the creation of targeted treatments or immunotherapies. These precision treatment strategies might significantly enhance effectiveness while minimizing side effects.

In summary, our findings present innovative approaches to overcoming tumors' drug resistance and provide a scientific basis for developing personalized treatment strategies.

3.4. Evaluation of treatment efficacy and immune cell distribution

To directly compare the efficacy of different therapeutic strategies, we analyzed the simulation results from the untreated group and the three treatment groups. Figure 9 shows the boxplots of cell populations at Day 60 for each group. The results demonstrate that all three treatments significantly reduce tumor cell counts compared with the untreated controls (Figure 9A). By Day 60, tumor cell numbers decrease to 30%–60% of the baseline values across treatments. Targeted therapy shows the strongest tumor growth suppression, followed by radiotherapy and immunotherapy.

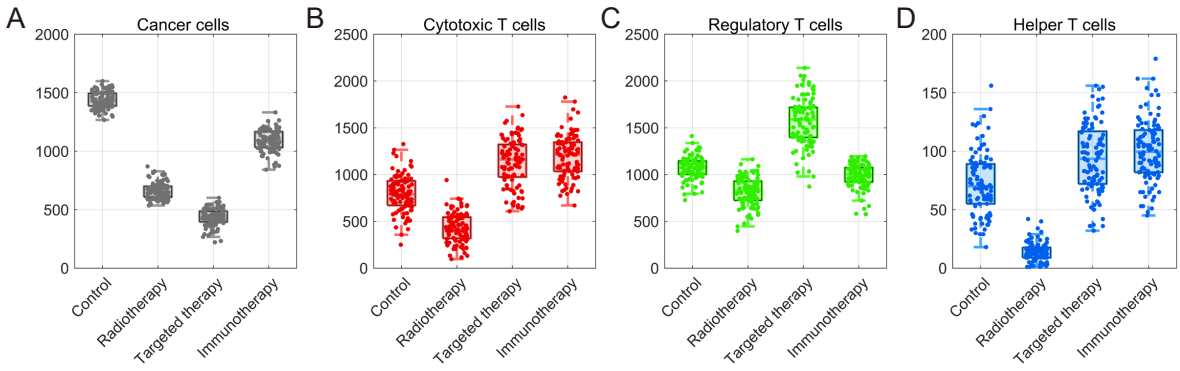

Figure 9. Cell population comparisons under different treatment modalities at Day 60. (A) Tumor cell count. (B) Cytotoxic T cell count. (C) Regulatory T cell count. (D) Helper T cell count.

Radiotherapy significantly reduced immune capacity in the TME (Figure 9B–D). In contrast, targeted therapy and immunotherapy promote immune cells' proliferation, particularly an increase in CTLs. Notably, immunotherapy not only substantially increases CTLs' and Th cells' proliferation but also effectively controls Tregs' expansion. These outcomes validate the immunoregulatory mechanisms encoded in our model, whereby immunotherapy enhances effector T cells' function while suppressing immunosuppressive cell activity. The consistency between the simulation results and the expected biological behavior confirms the model's capability to recapitulate tumor–immune interactions, thereby establishing a reliable foundation for subsequent investigations into combination treatment strategies.

To evaluate the therapeutic efficacy, we implement a tumor response classification system analogous to the Response Evaluation Criteria in Solid Tumors (RECIST 1.1) [58], categorizing the tumor response into four types on the basis of tumor cell counts: Progressive disease (PD), stable disease (SD), partial

response (PR), and complete response (CR). The classification rules are detailed as follows:

$$\begin{cases} \text{PD}, & C_{60} \geq (1+0.20)C_0, \\ \text{SD}, & (1-0.30)C_0 \leq C_{60} < (1+0.20)C_0, \\ \text{PR}, & (1-0.80)C_0 \leq C_{60} < (1-0.30)C_0, \\ \text{CR}, & C_{60} < (1-0.80)C_0. \end{cases} \tag{3.1}$$

Here, C_0 denotes the tumor cell count at $t = 0$, and C_{60} denotes the tumor cell count at $t = 60$.

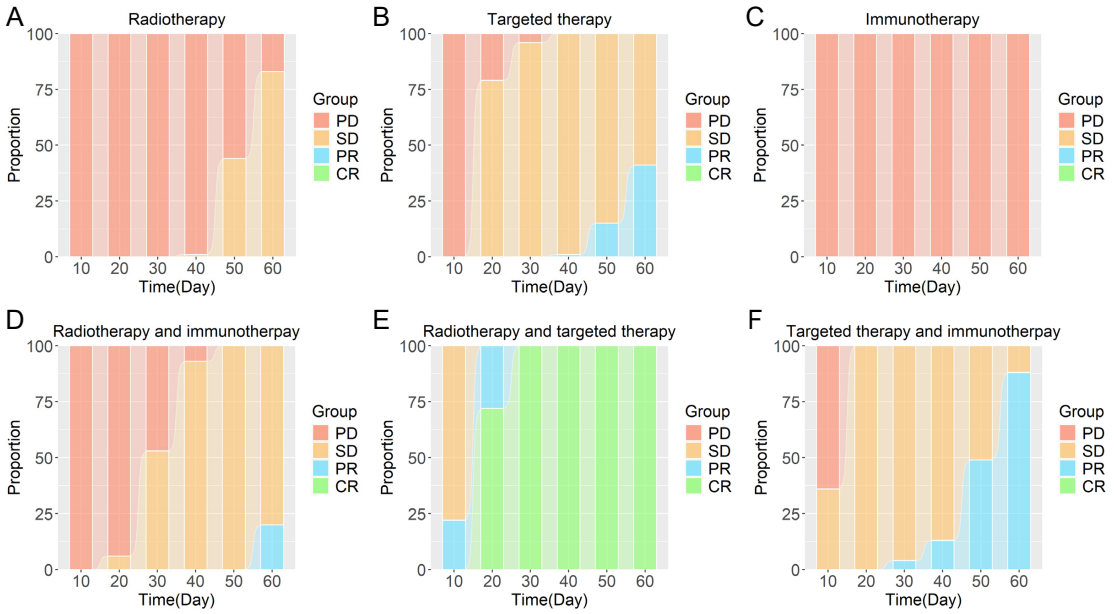

Figure 10. Therapeutic efficacy evaluation under monotherapies and combination therapies. (A) Radiotherapy. (B) Targeted therapy. (C) Immunotherapy. (D) Radiotherapy plus immunotherapy. (E) Radiotherapy plus targeted therapy. (F) Targeted therapy plus immunotherapy.

We performed 100 stochastic simulations for each of the combination therapies and calculated the proportions to achieve different tumor responses. The simulation results demonstrate that all treatment modalities inhibit tumor progression to varying degrees (Figure 10 and Table 2). Among monotherapies, targeted therapy shows the fastest response, with approximately 80% of the simulations achieving SD by Day 20, and over 37% reaching PR by the treatment's endpoint (Figure 10B). Radiotherapy exhibits a slower response, with SD beginning at Day 50 and predominating in the majority of simulations (Figure 10A). Immunotherapy consistently results in PD (Figure 10C).

Among the combination therapies, radiotherapy plus targeted therapy shows the best efficacy (Figure 10E and Table 2). Tumor growth is effectively controlled within 10 days, with over 20% of the simulations reaching PR directly (Figure 10E). By Day 30, all simulations achieve CR and maintain this status throughout the simulation. The other two combinations sequentially reached SD and ultimately PR (Figure 10D,F), with targeted therapy plus immunotherapy showing a faster onset.

The comparative analysis of all six treatment strategies reveals that combination therapies generally demonstrate significantly superior efficacy over monotherapies. These results suggest that when the

patient's conditions permit, combination therapies can shorten the treatment duration and substantially improve clinical outcomes. These findings provide critical evidence for optimizing clinical strategies and indicate broad application prospects for combination therapies in oncology.

Table 2. Therapeutic outcomes.

Treatment modalities	Tumor reduction ($C_5 - C_{60}$)	$\frac{N_{Tc}}{N_C}$ (Day 60)	Response categories (Day 60)			
			PD	SD	PR	CR
Control	−284	0.56	-	-	-	-
Radiotherapy	499	0.65	17%	83%	0%	0%
Targeted therapy	735	2.66	0%	59%	41%	0%
Immunotherapy	71	1.11	100%	0%	0%	0%
Radiotherapy plus immunotherapy	681	1.35	0%	80%	20%	0%
Radiotherapy plus targeted therapy	1149	328.82	0%	0%	0%	100%
Targeted therapy plus immunotherapy	793	4.23	0%	12%	88%	0%

3.5. Tumor progression under different treatment strengths

To further investigate the dynamic evolution of the tumor–immune system under different treatment intensities, we adjust three key therapeutic parameters: The radiotherapy-induced death rate coefficient $p^C_{dea,rad}$, the targeted therapy-induced death rate coefficient $p^C_{dea,tar}$, and the immunotherapy-induced death rate coefficient $p^C_{dea,ICI}$. Each treatment strategy is tested at five intensity levels, with 20 independent replicates per level. Treatment efficacy is evaluated by analyzing the averaged cell population dynamics (Figures 11–13). This approach enables a quantitative comparison of therapeutic efficacy across the strategies and their dynamic impacts on the TME.

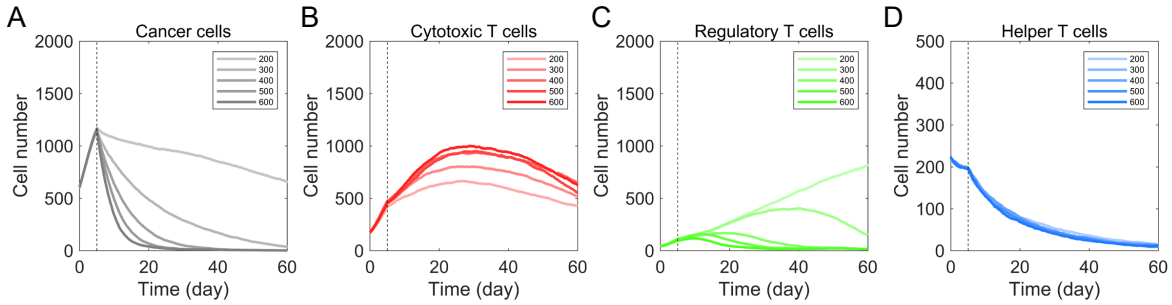

Figure 11. Dynamic evolution of the tumor–immune system under varying radiotherapy intensities. By adjusting the tumor cell radiosensitivity parameter $p^C_{dea,rad}$, we tested five parameter sets at intensities of 200, 300, 400, 500, and 600. (A) Tumor cells. (B) Cytotoxic T cells. (C) Regulatory T cells. (D) Helper T cells.

The simulation results show that after radiotherapy initiation, tumor cell depletion accelerates significantly with increasing treatment intensity (Figure 11A). When the tumoricidal efficacy parameter $p^C_{dea,rad}$ increases from 200 to 300, tumor cell numbers decrease substantially, but further increases in $p^C_{dea,rad}$ yield diminishing returns. For immune cells, higher radiotherapy intensity markedly elevates peak CTL counts (Figure 11B), while Th cell numbers remain largely unaffected (Figure 11D). Thus,

moderate intensity enhancement improves both tumor suppression and immune response in the TME. However, when $p^C_{dea,rad}$ increases from 400 to 600, complete tumor eradication occurs by Day 35 with parallel elimination of Tregs (Figure 11C), showing nearly identical depletion curves. These results suggest that maintaining $p^C_{dea,rad}$ below 400 preserves normal immune function while avoiding therapeutic saturation and excessive patient burden.

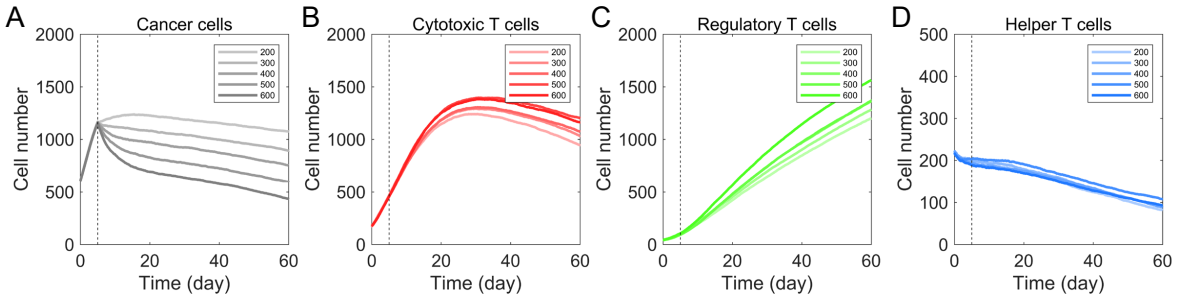

Figure 12. Dynamic evolution of the tumor–immune system under varying targeted therapy intensities. The regulatory coefficient $p^C_{dea,tar}$ for targeted therapy-induced tumor cell death is varied to simulate different treatment intensities, with five parameter values tested: $p^C_{dea,tar}$ = 200, 300, 400, 500, and 600. (A) Tumor cells. (B) Cytotoxic T cells. (C) Regulatory T cells. (D) Helper T cells.

Following targeted therapy initiation, tumor cell counts decrease consistently with increasing treatment intensity. Specifically, each 100 increment in $p^C_{dea,tar}$ reduces the final tumor cell counts by approximately 170, demonstrating effective tumor suppression (Figure 12A). Concurrently, immune cell populations increase variably with treatment intensity (Figure 12B–D). Notably, when $p^C_{dea,tar}$ reaches 600, CTL proliferation significantly increases. These results indicate that while targeted drugs directly kill tumor cells without explicitly regulating immune cell proliferation or apoptosis, they indirectly remodel the TME to enhance antitumor immunity.

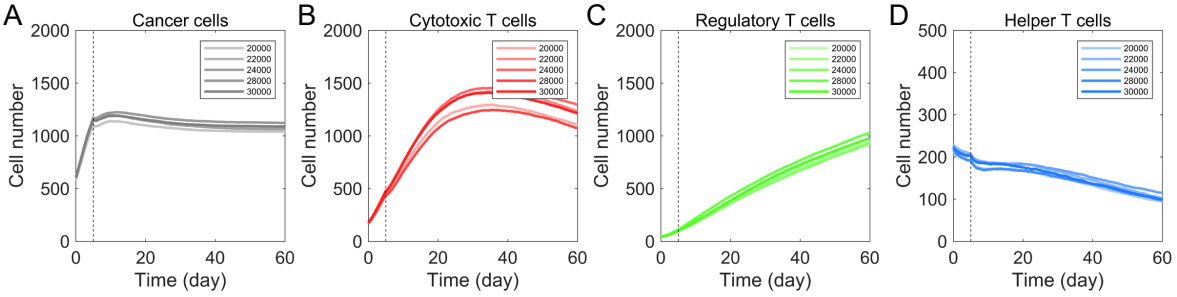

Figure 13. Dynamic evolution of the tumor–immune system under varying immunotherapy intensities. Different treatment intensities are simulated by adjusting the immunotherapy-induced tumor cell death rate coefficient $p^C_{dea,ICI}$, with five parameter sets: $p^C_{dea,ICI}$ = 20,000, 22,000, 24,000, 28,000, and 30,000. (A) Tumor cells. (B) Cytotoxic T cells. (C) Regulatory T cells. (D) Helper T cells.

Increasing immunotherapy intensity enhances tumor growth inhibition (Figure 13A). Comparative analysis of tumor and immune cell populations reveals more pronounced effects on immune cells

(Figure 13B–D), particularly a significant increase in CTL numbers (Figure 13B), demonstrating that immunotherapy primarily suppresses tumors by improving immune activity in the TME. Notably, when $p^C_{dea,ICI}$ ranges from 20,000 to 30,000, Treg and Th cell counts show minimal variation with treatment intensity (Figure 13C, D), suggesting an intensity threshold beyond which dose escalation may not further improve efficacy. These results suggest that optimal dosing should strike a balance between therapeutic effects and potential adverse events to prevent overtreatment.

3.6. Differential impact of drug sensitivity and development of resistance on therapeutic efficacy

To quantify the robustness of therapeutic outcomes to tumor heterogeneity, we evaluated how intrinsic tumor characteristics determine therapeutic efficacy, specifically the development of resistance and drug sensitivity thresholds. In clinical settings, patients' responses are often stratified by the extent of reduction in tumor burden. Accordingly, we defined therapeutic efficacy (E) as the relative reduction in tumor burden at Day 60 compared with the pretreatment baseline

$$E = \frac{C_{\text{pre}} - C_{\text{post}}}{C_{\text{pre}}} \times 100\%, \tag{3.2}$$

where C_{pre} and C_{post} represent the tumor cell counts before treatment and at Day 60, respectively. We performed extensive simulations to calculate E under varying combinations of drug resistance thresholds (x_0 for targeted therapy, y_0 for immunotherapy) and development of resistance rates (η_1, η_2). To ensure statistical reliability and account for the stochastic nature of the model, each parameter combination was evaluated using 10 independent simulations.

Figure 14 illustrates the relationship between the model's parameters and clinical outcomes. The results indicate that therapeutic efficacy is predominantly determined by drug sensitivity thresholds. As shown in Figure 14A,B, increasing the thresholds (x_0 and y_0) results in a monotonic and substantial increase in efficacy. Higher thresholds broaden the spectrum of tumor cells that are susceptible to treatment, effectively simulating a scenario in which the tumor is intrinsically more sensitive to the drug or the effective dosage is optimized to overcome resistance. For instance, in targeted therapy (Figure 14A), increasing x_0 from 0.2 to 0.8 shifts the outcome from marginal tumor inhibition (stable disease) to significant regression (high efficacy). In the case of immunotherapy (Figure 14B), however, a saturation effect is observed. While an increase in y_0 from 0.2 to 0.5 triggers a critical reversal from tumor progression ($\approx -7\%$ efficacy) to tumor regression, further increasing y_0 to 0.8 yields limited additional benefit ($\approx 10\%$–15%). This indicates that while a minimum sensitivity threshold is essential to halt tumor growth, the efficacy of immunotherapy may hit a plateau due to other limiting factors, such as immune cells' infiltration dynamics.

In contrast to sensitivity thresholds, variations in development of resistance rates (represented by different colors within each group) exert a negligible impact on efficacy within the simulated 60-day window. The bar heights for different parameters for the development of resistance (η) within the same sensitivity group are nearly uniform. Furthermore, the error bars, which represent the standard deviation across 10 independent runs, show significant overlap. This indicates that the minor variations observed are likely attributable to stochastic noise rather than a systematic effect driven by updated drug resistance.

These findings suggest a distinct hierarchy among clinical factors: During the induction phase of therapy, the magnitude of drug sensitivity (represented by x_0, y_0) outweighs the rate of phenotypic

adaptation (η_i). While a high η is theoretically linked to the gradual evolution of resistance, its effect is slow-acting. In contrast, the sensitivity threshold acts as an immediate "gatekeeper" of efficacy. Therefore, clinical strategies should prioritize optimizing drug selection and dosage to maximize the sensitivity match rather than targeting the mechanisms of the development of resistance in the early stages of treatment.

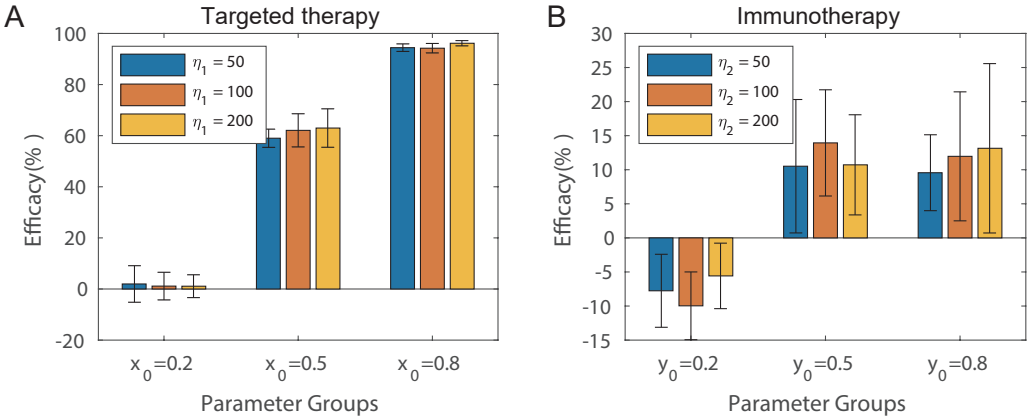

Figure 14. Therapeutic efficacies with varying sensitivity thresholds and drug resistance update rates. (A) Efficacy of targeted therapy across three sensitivity thresholds ($x_0 = 0.2, 0.5, 0.8$). (B) Efficacy of immunotherapy across three sensitivity thresholds ($y_0 = 0.2, 0.5, 0.8$). Within each group, different colored bars represent increasing values of the drug resistance update rates (η_1 or η_2). Data are presented as the mean ± SD for $n = 10$ independent simulations. The results highlight that efficacy is primarily driven by sensitivity thresholds, with immunotherapy showing a response plateau at higher thresholds ($y_0 \geq 0.5$), while the impact of the development of resistance remains statistically insignificant in the short term.

3.7. Parameter sensitivity analysis

To comprehensively evaluate the influence of the model's parameters on the predicted outcomes, we performed a local sensitivity analysis of non-treatment-related parameters governing cell proliferation and death. A total of 15 baseline parameters were selected, including the baseline death and proliferation rates of tumor cells, CTLs, Th cells, and Tregs. Under treatment-free conditions, each parameter was individually increased by a factor of two or decreased by half, while keeping all other parameters at their baseline values. For each parameter perturbation, 10 independent stochastic simulations were conducted to ensure statistical robustness. The sensitivity metric was defined as the mean relative change in tumor cell count at Day 60 compared with the baseline simulation: For parameter increases, the sensitivity was calculated as $S_+ = \text{mean}((Q_1 - Q)/Q)$, and for parameter decreases, as $S_- = \text{mean}((Q_2 - Q)/Q)$, where Q represents the tumor cell count at Day 60 under the baseline parameters, and Q_1 and Q_2 denote the tumor cell counts from 10 simulations with increased and decreased parameter values, respectively.

The sensitivity analysis revealed substantial variation in the influence of different parameters on the model's outputs (Figure 15). Multiple parameters associated with tumor cells and CTLs exhibited high sensitivity, with several showing absolute sensitivity values exceeding 0.1. First, the baseline

proliferation rate of tumor cells, $p^{C}_{pro,base}$, demonstrated a particularly strong impact on tumor cell count: Increasing this parameter led to a marked increase in tumor burden (a sensitivity of approximately 0.34), while decreasing it resulted in a substantial reduction (approximately −0.18). This indicates that the intrinsic proliferative capacity of tumor cells is a key determinant of the tumor burden. Second, tumor cell counts exhibited pronounced responses to perturbations in CTL-related parameters. On one hand, upregulation of CTL death parameters (e.g., $p^{T_c}_{dea,C}$ and $p^{T_c}_{dea,T_r}$, red bars) significantly increased tumor cell numbers, suggesting that these parameters indirectly regulate tumor growth by influencing CTLs' survival. On the other hand, downregulation of CTLs' proliferation parameters (e.g., $p^{T_c}_{pro,T_h}$, blue bars) also resulted in a marked increase in tumor cell counts, further confirming the critical role of Th cell-mediated promotion of CTL proliferation and the importance of CTLs' proliferative capacity in antitumor immunity. Additionally, the tumor cell death parameter regulated by CTLs, p^{C}_{dea,T_c}, exhibited strong negative sensitivity: Increasing this parameter reduced tumor burden, while decreasing it elevated tumor burden, a finding consistent with biological expectations. In summary, the model's predictions are particularly sensitive to the functional status of CTLs and the baseline proliferation and death rates of tumor cells. In future model calibration and clinical applications, priority should be given to the appropriate parameterization and uncertainty analysis of these key determinants.

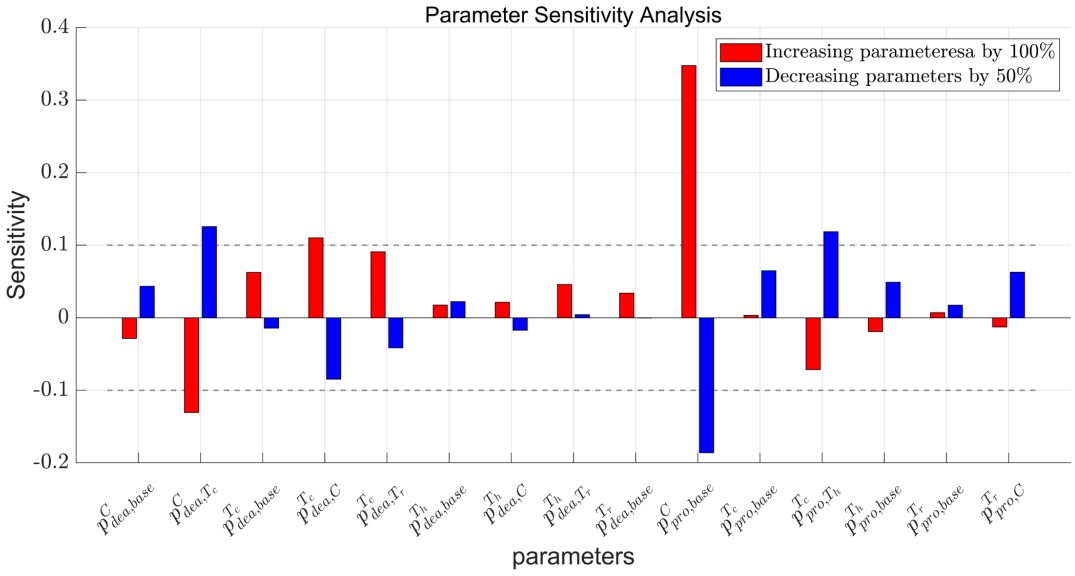

Figure 15. Parameter sensitivity analysis. Local sensitivity analysis of parameters related to cell death and proliferation under treatment-free conditions.

4. Discussion

In this study, we developed an agent-based, two-dimensional tumor–immune model that incorporates cellular heterogeneity as a key determinant of cell behavior and intercellular interactions. This computational framework simulates the spatiotemporal evolution of tumor–immune dynamics under various therapeutic interventions. We first characterized the natural evolutionary patterns of the untreated TME, followed by a systematic evaluation of both monotherapies and combination therapies. Subsequent

investigations elucidated the dynamic emergence of drug resistance during treatment. These results not only clarify the underlying mechanisms of resistance but also quantify the relationship between treatment intensity and therapeutic efficacy, providing a critical theoretical foundation for optimizing clinical regimens and overcoming resistance.

Extensive studies have demonstrated that the immune system plays a pivotal role in tumor development and treatment [3]. Previous research has utilized multiscale modeling to investigate tumor–immune interactions under diverse therapeutic strategies [16–18, 20, 21, 59], underscoring the utility of ABMs in capturing tumors' evolutionary dynamics. However, existing studies exhibit three primary limitations: (1) Oversimplified immune cell configurations that often lack immunosuppressive components such as Tregs; (2) insufficient consideration of how cellular heterogeneity modulates cell–cell interactions; and (3) a predominant focus on single-drug resistance mechanisms, with limited systematic comparison of combinatorial strategies. To bridge these gaps, our model integrates cellular heterogeneity with a diverse repertoire of immune cell types, thereby simulating the TME with greater physiological fidelity.

A critical quantitative insight derived from our simulations is the distinct hierarchy between intrinsic drug sensitivity and the development of resistance in determining therapeutic efficacy. While the development of resistance is frequently identified as a driver of long-term adaptation and the evolution of resistance, our results (specifically regarding the efficacy thresholds x_0 and y_0) demonstrate that intrinsic sensitivity acts as the primary "gatekeeper" of short-term therapeutic success. We observed that variations in the sensitivity thresholds induce substantial shifts in reductions in the tumor burden, where the rates of the development of resistance exert a negligible impact within the initial treatment window. Furthermore, the saturation effect observed in immunotherapy scenarios indicates that therapeutic efficacy is constrained not only by the tumor's immunogenicity but also by physical and spatial barriers. These barriers include limited immune cell infiltration rates and contact-dependent cytotoxicity caps imposed by the TME. We acknowledge that the current grid-based model has inherent limitations in capturing contact-dependent behaviors and biomechanical effects. Therefore, the abovementioned inferences regarding spatial constraints warrant further validation using more biophysically realistic modeling frameworks. This underscores the clinical imperative of prioritizing "sensitivity matching" (dose and drug selection) during the induction phase, while strategies targeting development of resistance may be more relevant for long-term maintenance to prevent acquired resistance.

Nonetheless, the current model still presents several limitations. First, the model primarily focuses on cellular-scale dynamics, simplifying tumor–immune interactions by omitting key molecular-level cytokines and their regulatory networks. It also excludes other important components of the TME, including cancer-associated fibroblasts, extracellular matrix macromolecules, and native nontumor cells. These components may influence cellular behavior through various mechanisms, such as chemokine or chemical gradients regulating cell migration and modulating the therapeutic response. Second, the grid-based implementation has three inherent limitations: Cell movement is restricted to discrete directions, the spatial carrying capacity is fixed, and biomechanical effects are difficult to incorporate. These effects, such as dynamic changes in extracellular matrix stiffness and cell stiffness [60–62], play a critical role in tumor progression. Future work could use off-lattice modeling approaches to overcome these limitations [25, 26, 62]. Third, the model currently lacks systematic integration with clinical data, from parameter calibration for specific cancer types to validation of the simulation against empirical datasets, which constrains its direct clinical translational potential. Fourth, constrained by computational resources and model complexity, the current simulations are confined to two-dimensional

space. However, three-dimensional modeling would more faithfully reflect *in vivo* tumor characteristics such as chemotactic gradients and diffusion resistance.

To address these limitations, we propose four directions for future model optimization.

(1) At the cellular level, we should incorporate additional TME components such as the extracellular matrix and its associated macromolecules, along with resident nontumor cells. At the molecular level, we can integrate differential equation models of the key signaling pathways involving cytokines and chemokines to more realistically simulate the complex regulatory effects of the TME on cellular behaviors such as proliferation, migration, and apoptosis. This approach enables a comprehensive analysis of the microenvironment's regulatory mechanisms.
(2) Drug mechanism incorporation: We can integrate pharmacokinetic/pharmacodynamic (PK/PD) models to precisely simulate drugs' absorption, distribution, and metabolism.
(3) Data-driven refinement: We can utilize single-cell RNA sequencing, spatial transcriptomics, and clinicopathological data to foster the development of patient-specific digital twins. This integration will enhance the parameters' realism and predictive accuracy, ultimately paving the way for personalized medicine strategies.
(4) Computational upgrade: We can develop a graphics processing unit (GPU) accelerated, three-dimensional ABM platform with parallel computing capabilities and interaction optimization for large-scale spatial simulations.

These enhancements will significantly increase the model's biological fidelity and computational performance, facilitating a robust tool for mechanistic investigation and the clinical translation of cancer immunotherapy.

Use of AI tools declaration

The authors declare they have not used artificial intelligence (AI) tools in the creation of this article.

Acknowledgments

This work is supported by the National Natural Science Foundation of China (NSFC 12331018).

Code availability

The codes used in this study are available at https://github.com/jinzhilei/ABM-tumor–immune-Dynamics.

Conflict of interest

Jinzhi Lei is an editorial board member for *Mathematical Biosciences and Engineering* and was not involved in the editorial review or the decision to publish this article. The authors declare there is no conflict of interest.

References

1. T. F. Gajewski, H. Schreiber, Y. X. Fu, Innate and adaptive immune cells in the tumor microenvironment, *Nat. Immunol.*, **14** (2013), 1014–1022. https://doi.org/10.1038/ni.2703
2. M. S. Paul, P. S. Ohashi, The roles of CD8(+) T cell subsets in antitumor immunity, *Trends Cell Biol.*, **30** (2020), 695–704. https://doi.org/10.1016/j.tcb.2020.06.003
3. K. E. de Visser, J. A. Joyce, The evolving tumor microenvironment: From cancer initiation to metastatic outgrowth, *Cancer Cell*, **41** (2023), 374–403. https://doi.org/10.1016/j.ccell.2023.02.016
4. C. Galassi, T. A. Chan, I. Vitale, L. Galluzzi, The hallmarks of cancer immune evasion, *Cancer Cell*, **42** (2024), 1825–1863. https://doi.org/10.1016/j.ccell.2024.09.010
5. A. Kashyap, M. A. Rapsomaniki, V. Barros, A. Fomitcheva-Khartchenko, A. L. Martinelli, A. F. Rodriguez, et al., Quantification of tumor heterogeneity: From data acquisition to metric generation, *Trends Biotechnol.*, **40** (2022), 647–676. https://doi.org/10.1016/j.tibtech.2021.11.006
6. J. Hausser, U. Alon, Tumour heterogeneity and the evolutionary trade-offs of cancer, *Nat. Rev. Cancer*, **20** (2020), 247–257. https://doi.org/10.1038/s41568-020-0241-6
7. S. Turajlic, A. Sottoriva, T. Graham, C. Swanton, Resolving genetic heterogeneity in cancer, *Nat. Rev. Genet.*, **20** (2019), 404–416. https://doi.org/10.1038/s41576-019-0114-6
8. R. A. Gatenby, J. S. Brown, Integrating evolutionary dynamics into cancer therapy, *Nat. Rev. Clin. Oncol.*, **17** (2020), 675–686. https://doi.org/10.1038/s41571-020-0411-1
9. J. C. Marine, S. J. Dawson, M. A. Dawson, Non-genetic mechanisms of therapeutic resistance in cancer, *Nat. Rev. Cancer*, **20** (2020), 743–756. https://doi.org/10.1038/s41568-020-00302-4
10. N. Vasan, J. Baselga, D. M. Hyman, A view on drug resistance in cancer, *Nature*, **575** (2019), 299–309. https://doi.org/10.1038/s41586-019-1730-1
11. Z. D. Shi, K. Pang, Z. X. Wu, Y. Dong, L. Hao, J. X. Qin, et al., Tumor cell plasticity in targeted therapy-induced resistance: mechanisms and new strategies, *Sig. Transduct. Target. Ther.*, **8** (2023), 113. https://doi.org/10.1038/s41392-023-01383-x
12. G. Albi, R. Chignola, F. Ferrarese, Efficient ensemble stochastic algorithms for agent-based models with spatial predator–prey dynamics, *Math. Comput. Simul.*, **199** (2022), 317–340. https://doi.org/10.1016/j.matcom.2022.03.019
13. J. Metzcar, Y. Wang, R. Heiland, P. Macklin, A review of cell-based computational modeling in cancer biology, *JCO Clin. Cancer Inf.*, **3** (2019), 1–13. https://doi.org/10.1200/CCI.18.00069
14. E. Merelli, G. Armano, N. Cannata, F. Corradini, M. d'Inverno, A. Doms, et al., Agents in bioinformatics, computational and systems biology, *Briefings Bioinf.*, **8** (2007), 45–59. https://doi.org/10.1093/bib/bbl014
15. L. Zhang, Z. Wang, J. A. Sagotsky, T. S. Deisboeck, Multiscale agent-based cancer modeling, *J. Math. Biol.*, **58** (2009), 545–559. https://doi.org/10.1007/s00285-008-0211-1
16. M. N. G. van Genderen, J. Kneppers, A. Zaalberg, E. M. Bekers, A. M. Bergman, W. Zwart, et al., Agent-based modeling of the prostate tumor microenvironment uncovers spatial tumor growth constraints and immunomodulatory properties, *NPJ Syst. Biol. Appl.*, **10** (2024), 20. https://doi.org/10.1038/s41540-024-00344-6

17. A. R. Anderson, A. M. Weaver, P. T. Cummings, V. Quaranta, Tumor morphology and phenotypic evolution driven by selective pressure from the microenvironment, *Cell*, **127** (2006), 905–915. https://doi.org/10.1016/j.cell.2006.09.042

18. L. Zhang, L. L. Chen, T. S. Deisboeck, Multi-scale, multi-resolution brain cancer modeling, *Math. Comput. Simul.*, **79** (2009), 2021–2035. https://doi.org/10.1016/j.matcom.2008.09.007

19. G. Stamatakos, D. Dionysiou, A. Lunzer, R. Belleman, E. Kolokotroni, E. Georgiadi, et al., The technologically integrated oncosimulator: Combining multiscale cancer modeling with information technology in the in silico oncology context, *IEEE J. Biomed. Health Inf.*, **18** (2014), 840–854. https://doi.org/10.1109/JBHI.2013.2284276

20. C. Gong, O. Milberg, B. Wang, P. Vicini, R. Narwal, L. Roskos, et al., A computational multiscale agent-based model for simulating spatio-temporal tumour immune response to PD1 and PDL1 inhibition, *J. R. Soc. Interface*, **14** (2017), 20170320. https://doi.org/10.1587/elex.14.20170320

21. A. Jalalimanesh, H. S. Haghighi, A. Ahmadi, M. Soltani, Simulation-based optimization of radiotherapy: Agent-based modeling and reinforcement learning, *Math. Comput. Simul.*, **133** (2017), 235–248. https://doi.org/10.1016/j.matcom.2016.05.008

22. J. U. Legaria-Peña, F. Sánchez-Morales, Y. Cortés-Poza, Evaluation of entropy and fractal dimension as biomarkers for tumor growth and treatment response using cellular automata, *J. Theor. Biol.*, **564** (2023), 111462. https://doi.org/10.1016/j.jtbi.2023.111462

23. J. U. Legaria-Peña, F. Sánchez-Morales, Y. Cortés-Poza, Understanding post-angiogenic tumor growth: Insights from vascular network properties in cellular automata modeling, *Chaos, Solitons Fractals*, **186** (2024), 115199. https://doi.org/10.1016/j.chaos.2024.115199

24. J. U. Legaria-Peña, F. Sánchez-Morales, Y. Cortés-Poza, Study of the interplay between cancer, inflammation, and immune disorders: A cellular automaton approach, *Appl. Math. Model.*, **150** (2026), 116315. https://doi.org/10.1016/j.apm.2025.116315

25. A. Surendran, A. L. Jenner, E. Karimi, B. Fiset, D. F. Quail, L. A. Walsh, et al., Agent-based modelling reveals the role of the tumor microenvironment on the short-term success of combination temozolomide/immune checkpoint blockade to treat glioblastoma, *J. Pharmacol. Exp. Ther.*, **387** (2023), 66–77. https://doi.org/10.1124/jpet.122.001571

26. B. Mongeon, J. Hébert-Doutreloux, A. Surendran, E. Karimi, B. Fiset, D. F. Quail, et al., Spatial computational modelling illuminates the role of the tumour microenvironment for treating glioblastoma with immunotherapies, *NPJ Syst. Biol. Appl.*, **10** (2024), 91. https://doi.org/10.1038/s41540-024-00419-4

27. J. West, M. Robertson-Tessi, A. R. Anderson, Agent-based methods facilitate integrative science in cancer, *Trends Cell Biol.*, **33** (2023), 300–311. https://doi.org/10.1016/j.tcb.2022.10.006

28. D. Hanahan, R. A. Weinberg, The hallmarks of cancer, *Cell*, **100** (2000), 57–70. https://doi.org/10.1016/S0092-8674(00)81683-9

29. D. Hanahan, R. A. Weinberg, Hallmarks of cancer: The next generation, *Cell*, **144** (2011), 646–674. https://doi.org/10.1016/j.cell.2011.02.013

30. D. Hanahan, Hallmarks of cancer: New dimensions, *Cancer Discov.*, **12** (2022), 31–46. https://doi.org/10.1158/2159-8290.CD-21-1059

31. H. Raskov, A. Orhan, J. P. Christensen, I. Gögenur, Cytotoxic CD8+ T cells in cancer and cancer immunotherapy, *Br. J. Cancer*, **124** (2020), 359–367. https://doi.org/10.1038/s41416-020-01048-4

32. M. Philip, A. Schietinger, CD8+ T cell differentiation and dysfunction in cancer, *Nat. Rev. Immunol.*, **22** (2021), 209–223. https://doi.org/10.1057/s41260-021-00210-8

33. J. R. Giles, A. M. Globig, S. M. Kaech, E. J. Wherry, CD8+ T cells in the cancer-immunity cycle, *Immunity*, **56** (2023), 2231–2253. https://doi.org/10.1016/j.immuni.2023.09.005

34. Z. Vasconcelos, S. Müller, D. Guipouy, W. Yu, C. Christophe, S. Gadat, et al., Individual human cytotoxic T lymphocytes exhibit intraclonal heterogeneity during sustained killing, *Cell Rep.*, **11** (2015), 1474–1485. https://doi.org/10.1016/j.celrep.2015.05.002

35. R. Khazen, M. Cazaux, F. Lemaître, B. Corre, Z. Garcia, P. Bousso, Functional heterogeneity of cytotoxic T cells and tumor resistance to cytotoxic hits limit anti-tumor activity *in vivo*, *EMBO J.*, **40** (2021), e106658. https://doi.org/10.15252/embj.2020106658

36. D. H. Raulet, M. J. Bevan, A differentiation factor required for the expression of cytotoxic T-cell function, *Nature*, **296** (1982), 754–757. https://doi.org/10.1038/296754a0

37. F. Y. Liew, Th1 and Th2 cells: A historical perspective, *Nat. Rev. Immunol.*, **2** (2002), 55–60. https://doi.org/10.1038/nri705

38. R. Spolski, P. Li, W. J. Leonard, Biology and regulation of IL-2: From molecular mechanisms to human therapy, *Nat. Rev. Immunol.*, **18** (2018), 648–659. https://doi.org/10.1038/s41577-018-0046-y

39. T. Okazaki, S. Chikuma, Y. Iwai, S. Fagarasan, T. Honjo, A rheostat for immune responses: The unique properties of PD-1 and their advantages for clinical application, *Nat. Immunol.*, **14** (2013), 1212–1218. https://doi.org/10.1038/ni.2762

40. N. Patsoukis, Q. Wang, L. Strauss, V. A. Boussiotis, Revisiting the PD-1 pathway, *Sci. Adv.*, **6** (2020), eabd2712. https://doi.org/10.1126/sciadv.abd2712

41. W. Zou, Regulatory T cells, tumour immunity and immunotherapy, *Nat. Rev. Immunol.*, **6** (2006), 295–307. https://doi.org/10.1038/nri1806

42. A. Facciabene, G. T. Motz, G. Coukos, T-regulatory cells: Key players in tumor immune escape and angiogenesis, *Cancer Res.*, **72** (2012), 2162–2171. https://doi.org/10.1158/0008-5472.CAN-11-3687

43. Y. Togashi, K. Shitara, H. Nishikawa, Regulatory T cells in cancer immunosuppression—implications for anticancer therapy, *Nat. Rev. Clin. Oncol.*, **16** (2019), 356–371. https://doi.org/10.1038/s41571-019-0175-7

44. C. J. Imianowski, Q. Chen, C. J. Workman, D. A. A. Vignali, Regulatory T cells in the tumour microenvironment, *Nat. Rev. Cancer*, **25** (2025), 703–722. https://doi.org/10.1038/s41568-025-00832-9

45. L. Zhou, M. M. Chong, D. R. Littman, Plasticity of CD4+ T cell lineage differentiation, *Immunity*, **30** (2009), 646–655. https://doi.org/10.1016/j.immuni.2009.05.001

46. A. J. Ozga, M. T. Chow, A. D. Luster, Chemokines and the immune response to cancer, *Immunity*, **54** (2021), 859–874. https://doi.org/10.1016/j.immuni.2021.01.012.

47. N. Nagarsheth, M. S. Wicha, W. Zou, Chemokines in the cancer microenvironment and their relevance in cancer immunotherapy, *Nat. Rev. Immunol.*, **17** (2017), 559–572. https://doi.org/10.1038/nri.2017.49

48. J. A. Joyce, D. T. Fearon, T cell exclusion, immune privilege, and the tumor microenvironment, *Science*, **348** (2015), 74–80. https://doi.org/10.1126/science.aaa6204

49. D. De Ruysscher, G. Niedermann, N. G. Burnet, S. Siva, A. W. M. Lee, F. Hegi-Johnson, Radiotherapy toxicity, *Nat. Rev. Dis. Primers*, **5** (2019), 13. https://doi.org/10.1038/s41572-019-0068-1

50. R. A. Chandra, F. K. Keane, F. E. M. Voncken, C. R. J. Thomas, Contemporary radiotherapy: Present and future, *Lancet*, **398** (2021), 171–184. https://doi.org/10.1016/S0140-6736(21)00233-6

51. A. C. Begg, F. A. Stewart, C. Vens, Strategies to improve radiotherapy with targeted drugs, *Nat. Rev. Cancer*, **11** (2011), 239–253. https://doi.org/10.1038/nrc3007

52. H. E. Barker, J. T. E. Paget, A. A. Khan, K. J. Harrington, The tumour microenvironment after radiotherapy: Mechanisms of resistance and recurrence, *Nat. Rev. Cancer*, **15** (2015), 409–425. https://doi.org/10.1038/nrc3958

53. H. Y. Choi, J. E. Chang, Targeted therapy for cancers: From ongoing clinical trials to FDA-approved drugs, *Int. J. Mol. Sci.*, **24** (2023), 13618. https://doi.org/10.3390/ijms241713618

54. P. Ramos, M. Bentires-Alj, Mechanism-based cancer therapy: Resistance to therapy, therapy for resistance, *Oncogene*, **34** (2014), 3617–3626. https://doi.org/10.1038/onc.2014.314

55. C. Sun, R. Mezzadra, T. N. Schumacher, Regulation and function of the PD-L1 checkpoint, *Immunity*, **48** (2018), 434–452. https://doi.org/10.1016/j.immuni.2018.03.014

56. C. Zhang, C. Shao, X. Jian, Y. Bai, M. Li, H. Shi, et al., Individual cell-based modeling of tumor cell plasticity-induced immune escape after CAR-T therapy, *Comput. Syst. Oncol.*, **1** (2021), e21029. https://doi.org/10.1002/cso2.1029

57. S. V. Sharma, D. Y. Lee, B. Li, M. P. Quinlan, F. Takahashi, S. Maheswaran, et al., A chromatin-mediated reversible drug-tolerant state in cancer cell subpopulations, *Cell*, **141** (2010), 69–80. https://doi.org/10.1016/j.cell.2010.02.027

58. E. Eisenhauer, P. Therasse, J. Bogaerts, L. Schwartz, D. Sargent, R. Ford, et al., New response evaluation criteria in solid tumours: Revised RECIST guideline (version 1.1), *Eur. J. Cancer*, **45** (2009), 228–247.

59. J. W. Hickey, E. Agmon, N. Horowitz, T. K. Tan, M. Lamore, J. B. Sunwoo, et al., Integrating multiplexed imaging and multiscale modeling identifies tumor phenotype conversion as a critical component of therapeutic T cell efficacy, *Cell Syst.*, **15** (2024), 322–338.e5. https://doi.org/10.1016/j.cels.2024.03.004

60. W. Xu, R. Mezencev, B. Kim, L. Wang, J. McDonald, T. Sulchek, Cell stiffness is a biomarker of the metastatic potential of ovarian cancer cells, *PLoS One*, **7** (2012), e46609. https://doi.org/10.1371/journal.pone.0046609

61. M. Najafi, B. Farhood, K. Mortezaee, Extracellular matrix (ECM) stiffness and degradation as cancer drivers, *J. Cell Biochem.*, **120** (2018), 2782–2790. https://doi.org/10.1002/jcb.27681

62. C. Borau, R. Chisholm, P. Richmond, D. Walker, An agent-based model for cell microenvironment simulation using FLAMEGPU2, *Comput. Biol. Med.*, **179** (2024), 108831. https://doi.org/10.1016/j.compbiomed.2024.108831

AIMS Press